

SPECTRAL ENERGY DISTRIBUTIONS OF TYPE 1 AGN IN THE COSMOS SURVEY I - THE XMM-COSMOS SAMPLE

M. ELVIS¹, H. HAO^{1, 2}, F. CIVANO¹, M. BRUSA³, M. SALVATO^{3,4,5}, A. BONGIORNO^{3,6}, P. CAPAK⁷, G. ZAMORANI⁸, A. COMASTRI⁸, K. JAHNKE⁹, E. LUSO⁹, V. MAINIERI¹⁰, J. R. TRUMP^{11,12}, L. C. HO¹³, H. AUSSEL¹⁴, N. CAPPELLUTI^{3,8}, M. CISTERNAS⁹, D. FRAYER¹⁵, R. GILLI⁸, G. HASINGER¹⁶, J. P. HUCHRA^{11,17}, C. D. IMPEY¹¹, A. M. KOEKEMOER¹⁸, G. LANZUISI^{1,3,19, 20}, E. LE FLOC'H²¹, S. J. LILLY²², Y. LIU²³, P. MCCARTHY¹³, H. J. MCCrackEN²⁴, A. MERLONI³, H.-J. ROESER⁹, D. B. SANDERS¹⁶, M. SARGENT^{9, 21}, N. SCOVILLE⁷, E. SCHINNERER⁹, D. SCHIMINOVICH²⁵, J. SILVERMAN²⁶, Y. TANIGUCHI²⁷, C. VIGNALI²⁸, C. M. URRY²⁹, M. A. ZAMOJSKI²⁵, M. ZATLOUKAL⁹

version: Aug 19th, 2012. revised for ApJ referee

ABSTRACT

The “Cosmic Evolution Survey” (COSMOS) enables the study of the Spectral Energy Distributions (SEDs) of Active Galactic Nuclei (AGN) because of the deep coverage and rich sampling of frequencies from X-ray to radio. Here we present a SED catalog of 413 X-ray (*XMM-Newton*) selected type 1 (emission line FWHM > 2000 km s⁻¹) AGN with Magellan, SDSS or VLT spectrum. The SEDs are corrected for the Galactic extinction, for broad emission line contributions, constrained variability, and for host galaxy contribution. We present the mean SED and the dispersion SEDs after the above corrections in the rest frame 1.4 GHz to 40 keV, and show examples of the variety of SEDs encountered. In the near-infrared to optical (rest frame $\sim 8\mu\text{m} - 4000\text{\AA}$), the photometry is complete for the whole sample and the mean SED is derived from detections only. Reddening and host galaxy contamination could account for a large fraction of the observed SED variety. The SEDs are all available on-line.

Subject headings: galaxies: evolution; quasars: general; surveys

elvis@cfa.harvard.edu, hhao@cfa.harvard.edu

¹ Harvard Smithsonian Center for astrophysics, 60 Garden St., Cambridge, MA 02138, USA

² SISSA, Via Bonomea 265, I-34136 Trieste, Italy

³ Max Planck Institute für Extraterrestrische Physik, Postfach 1312, 85741, Garching bei München, Germany

⁴ IPP - Max-Planck-Institute for Plasma Physics, Boltzmann Strasse 2, D-85748, Garching bei München, Germany

⁵ Excellence Cluster, Boltzmann Strasse 2, D-85748, Garching bei München, Germany

⁶ INAF-Osservatorio Astronomico di Roma, Via di Frascati 33, 00040, Monteporzio Catone, Rome, Italy

⁷ California Institute of Technology, MC 105-24, 1200 East California Boulevard, Pasadena, CA 91125, USA

⁸ INAF-Osservatorio Astronomico di Bologna, via Ranzani 1, I-40127 Bologna, Italy

⁹ Max Planck Institute für Astronomie, Königstuhl 17, Heidelberg, D-69117, Germany

¹⁰ European Southern Observatory, Karl-Schwarzschild-Strasse 2, D-85748 Garching bei München, Germany

¹¹ Steward Observatory, University of Arizona, 933 North Cherry Avenue, Tucson, AZ 85721, USA

¹² UCO/Lick Observatory, University of California, Santa Cruz, CA 95064, USA

¹³ The Observatories of the Carnegie Institute for Science, Santa Barbara Street, Pasadena, CA 91101, USA

¹⁴ AIM Unité Mixte de Recherche CEA CNRS, Université Paris VII UMR n158, Paris, France

¹⁵ National Radio Astronomy Observatory, P.O. Box 2, Green Bank, WV 24944, USA

¹⁶ Institute for Astronomy, University of Hawaii, 2680 Woodlawn Drive, Honolulu, HI 96822, USA

¹⁷ John P. Huchra has contributed to the work before his death in October 2010.

¹⁸ Space Telescope Science Institute, 3700 San Martin Drive, Baltimore, MD 21218, USA

¹⁹ INAF-IASF Roma, Via Fosso del Cavaliere 100, 00133 Rome, Italy

²⁰ INAF-IASF Bologna, Via Gobetti 101, I-40129 Bologna, Italy

²¹ CEA-Saclay, Service d'Astrophysique, Orme des Merisiers, Bat. 709, 91191 Gif-sur-Yvette, France

²² Institute of Astronomy, Swiss Federal Institute of Technology (ETH Hönggerberg), CH-8093, Zürich, Switzerland

²³ Key Laboratory of Particle Astrophysics, Institute of High Energy Physics, Chinese Academy of Sciences, P.O. Box 918-3, Beijing 100049, China

²⁴ Institut d'Astrophysique de Paris, UMR 7095 CNRS, Université Pierre et Marie Curie, 98 bis Boulevard Arago, F-75014 Paris, France

²⁵ Department of Astronomy, Columbia University, MC2457, 550 W. 120 St. New York, NY 10027, USA

²⁶ Institute for the Physics and Mathematics of the Universe (IPMU), University of Tokyo, Kashiwanoha 5-1-5, Kashiwa-shi, Chiba 277-8568, Japan

²⁷ Research Center for Space and Cosmic Evolution, Ehime University, Bunkyo-cho 2-5, Matsuyama 790-8577, Japan

²⁸ Dipartimento di Astronomia, Università degli Studi di Bologna, via Ranzani 1, I-40127 Bologna, Italy

²⁹ Physics Department and Yale Center for Astronomy and Astrophysics, Yale University, New Haven, CT 06511, USA

1. INTRODUCTION

Quasars and Active Galactic Nuclei (AGN) are the most luminous persistent sources of radiation in the universe. The AGN luminosity is emitted primarily in a broad continuum spectrum that carries significant power over several decades, from the far-infrared (FIR) to the X-ray bands. Hence, knowing the spectral energy distributions (SEDs) of AGN is essential to a deeper understanding of quasar physics. The mean spectral energy distribution (SED) compiled by Elvis et al. (1994, “E94” hereinafter) is still the most commonly used SED for quasars, despite recent additions and updates (see e.g. Polletta et al. 2000, Kuraszekiewicz et al. 2003, Marconi et al. 2004, Risaliti & Elvis 2004, Richards et al. 2006, Hopkins et al. 2006, Polletta et al. 2007, Shang et al. 2011, Luo et al. 2010, Lusso et al. 2010, 2011). However the E94 SEDs suffer from significant limitations: (1) the sample is primarily an ultraviolet excess selected sample, and is further biased toward relatively X-ray loud quasars; (2) the mean SED was compiled from a small number of AGN (29 radio-quiet and 18 radio-loud AGN); (3) the sample only covers a low redshift range ($0.05 \leq z \leq 0.9$, with 80% being at $z < 0.3$); (4) the data in X-ray, ultraviolet and far infrared region have limited signal-to-noise ratios, with a large number of upper limits. Even so, E94 found a large dispersion in SEDs of ~ 1 dex at both $100 \mu\text{m}$ and $0.1 \mu\text{m}$, when all the SEDs were normalized at $1 \mu\text{m}$. The $1 \mu\text{m}$ wavelength is usually chosen as a normalization point because it is the approximate location of the inflection between the rising Wien tail of emission from hot dust and the power-law $f_\nu \propto \nu^{1/3}$ of the big blue bump in the optical caused by the emission of the accretion disk in νf_ν versus ν space (E94). This variety of continuum shapes in quasars has not been carefully explored so that no correlations of SED shape in the FIR-UV with other properties have been found, nor is there an accepted theoretical explanation fitting all the various forms.

The Cosmic Evolution Survey (COSMOS; Scoville et al. 2007a) has the appropriate combination of depth, area and multi-wavelength coverage that allows detection of substantial AGN samples by all standard techniques – X-ray (Brusa et al. 2007, 2010, Civano et al. 2012), infrared (Donley et al. 2012), radio (Schinnerer et al. 2010) and optical (Gabor et al. 2009). COSMOS covers a 2 deg^2 equatorial field centered on $RA = 10 : 00 : 28.6$, $Dec = +02 : 12 : 21$ (J2000) with deep imaging by most of the major space-based telescopes: *Hubble* (Scoville et al. 2007b, Koekemorer et al. 2007), *Spitzer* (Sanders et al. 2007, 2010), *GALEX* (Zamojski et al. 2007), *XMM-Newton* (Hasinger et al. 2007, Cappelluti et al. 2009), *Chandra* (Elvis et al. 2009), and large ground based telescopes: Subaru (Taniguchi et al. 2007), VLA (Schinnerer et al. 2007, 2010), CFHT (McCracken et al. 2007), UKIRT, NOAO (Capak et al. 2007). The imaging coverage is complemented by dedicated redshift surveys conducted with the VIMOS/VLT (zCOSMOS, Lilly et al. 2007, 2009), IMACS/Magellan (Trump et al. 2007, 2009a), DEIMOS/Keck³⁰, for a total of more than 20k spectra collected. The field has also been covered by

SDSS (Abazajian et al. 2004), for both photometry and spectroscopy.

COSMOS contains over 400 type 1 (i.e. broad emission line, $\text{FWHM} > 2000 \text{ km s}^{-1}$) AGN, spanning a wide range of redshifts, that were identified through the MMT/IMACS, zCOSMOS and SDSS surveys (Brusa et al. 2007, 2010). So far the COSMOS data set has 43 photometric bands, with high signal-to-noise ($\gtrsim 80$) for a typical $I=22.5$ type 1 AGN. Hence COSMOS overcomes the limitations of E94, offering an opportunity of making order of magnitude improvements in our knowledge of AGN SEDs.

This is the first of a series of papers on the SEDs of the X-ray selected type 1 AGN in COSMOS. The main goal of this study is to improve the type 1 AGN SED template over that of E94 and, perhaps more importantly, to study the diversity of AGN SEDs and their relation with physical parameters. Lusso et al. (2010), in a complementary paper, analyzed a sample of 545 *XMM-Newton* selected type 1 AGN in XMM-COSMOS, including both the spectroscopic (361/545) and photometric (184/545) identifications in order to study dependence on luminosity and redshift of the relationship between the UV and X-ray luminosity (α_{OX}). Trump et al. (2011) also presented SED information for 348 *XMM-Newton* selected AGN in COSMOS, although they focused on the differences between type 1 and unobscured type 2 AGN SEDs rather than the dispersion among type 1 AGN themselves. This paper (Paper I) describes the properties of the sample used for this study and presents the mean SED, including corrections for the Galactic extinction, broad emission line (BEL) contribution, while limiting both variability and host galaxy contamination. Other 3 companion papers on this subject are in preparation (Hao et al. 2012 a, b, c). The companion Paper II (Hao et al. 2012a) investigates the systematic trends in the shapes of the SED in the wavelength range of $0.3\text{--}3\mu\text{m}$ as a function of redshift, bolometric luminosity, black hole mass and Eddington ratio. Paper III (Hao et al. 2012b) introduces a “mixing diagram” (near-infrared SED slope versus optical SED slope plot) to understand the diversity of the SED shapes in XMM-COSMOS type 1 AGN sample, provide a new estimation of the host galaxy fraction and reddening, and identify interesting outliers. Paper IV (Hao et al. 2012c) studies the radio-loudness of the XMM-COSMOS type 1 AGN. An interesting subsample of “hot dust poor” quasars, drawn from this sample, have already been presented in Hao et al. (2010).

In this paper, all magnitudes are reported in the AB system (Oke & Gunn 1983) and the WMAP 5-year cosmology (Komatsu et al. 2009), with $H_0 = 71 \text{ km s}^{-1} \text{ Mpc}^{-1}$, $\Omega_M = 0.26$ and $\Omega_\Lambda = 0.74$ is assumed.

2. SAMPLE DESCRIPTION

X-ray emission is ubiquitous in AGN, and in the X-ray band, the obscuration and complication from host galaxy light are minimized. Hence X-ray surveys give the most complete and effective census of AGN of any single band (Risaliti & Elvis 2004). The XMM-COSMOS survey (Hasinger et al. 2007) observed the entire COSMOS field for a total of ~ 1.5 Ms, with an average exposure of 60 ks across the field to a depth of $\sim 5 \times 10^{-16} \text{ erg cm}^{-2} \text{ s}^{-1}$

³⁰ The result of a multi-year observing campaign (PIs: Capak, Kartaltepe, Salvato, Sanders, Scoville; see Kartaltepe et al. 2010).

TABLE 1
DATA QUALITY AND DEPTH

Filter Name	Telescope	Effective ¹ Wavelength(Å)	Filter ² Width(Å)	Depth ³	Number of Detections	Observations date	k_λ ⁴	A_λ ⁵
<i>X</i>	XMM	2keV	0.5-10keV	10^{-15} **	413	Dec 2003-May 2005		
<i>FUV</i>	Galex	1540	209	25.69	136	Feb 2004	8.92	0.17
<i>NUV</i>	Galex	2315	797	25.99	263	Feb 2004	7.97	0.15
<i>u</i>	SDSS	3564	600	22.00	370	Jul 2001*	4.69	0.09
<i>u*</i>	CFHT	3823	605	26.50	412	Jan 2003-Apr 2007	4.69	0.09
<i>IA427</i>	Subaru	4263	208	25.82	411	Jan 2006	4.21	0.08
<i>B_J</i>	Subaru	4458	897	27.00	413	Jan 2004	4.04	0.08
<i>IA464</i>	Subaru	4635	218	25.65	411	Feb 2006	3.86	0.07
<i>g</i>	SDSS	4723	1300	22.20	405	Jul 2001*	3.74	0.07
<i>g⁺</i>	Subaru	4777	1265	27.00	413	Feb 2004	3.74	0.07
<i>IA484</i>	Subaru	4849	229	25.60	410	Jan 2007	3.67	0.07
<i>IA505</i>	Subaru	5063	232	25.55	412	Feb 2006	3.45	0.07
<i>IA527</i>	Subaru	5261	243	25.62	410	Jan 2007	3.29	0.06
<i>V_J</i>	Subaru	5478	946	26.60	412	Feb 2004	3.15	0.06
<i>IA574</i>	Subaru	5765	273	25.61	412	Jan 2006	2.96	0.06
<i>r</i>	SDSS	6202	1200	22.00	401	Jul 2001*	2.59	0.05
<i>IA624</i>	Subaru	6233	300	25.60	410	Dec 2006	2.61	0.05
<i>r⁺</i>	Subaru	6289	1382	26.80	413	Jan 2004	2.59	0.05
<i>IA679</i>	Subaru	6781	336	25.60	412	Feb 2006	2.27	0.04
<i>IA709</i>	Subaru	7074	317	25.65	411	Jan 2006	2.15	0.04
<i>NB711</i>	Subaru	7120	73	25.00	412	Feb 2006	2.13	0.04
<i>IA738</i>	Subaru	7362	324	25.60	410	Jan 2007	2.04	0.04
<i>i</i>	SDSS	7523	1300	21.30	406	Jul 2001*	1.92	0.04
<i>i*</i>	CFHT	7618	1300	24.00	411	Jan 2004	1.92	0.04
<i>i⁺</i>	Subaru	7684	1495	26.20	199 ⁶	Jan 2004	1.92	0.04
<i>IA767</i>	Subaru	7685	364	25.60	412	Mar 2007	1.92	0.04
<i>F814W</i>	HST	8072	1830	27.10	388 ⁷	Oct 2003*	1.80	0.03
<i>NB816</i>	Subaru	8149	120	25.70	413	Feb 2005*	1.74	0.03
<i>IA827</i>	Subaru	8245	343	25.39	411	Jan 2006	1.69	0.03
<i>z</i>	SDSS	8905	1000	20.50	368	Jul 2001*	1.44	0.03
<i>z⁺</i>	Subaru	9037	856	25.20	411	Jan 2004	1.44	0.03
<i>J</i>	UH 88 ⁷	12491	1580	23.70	413	Mar 2006	0.97	0.02
<i>H</i>	Calar Alto	16483	2665	20.90	252	Aug 2005		
<i>K</i>	KPNO	21537	3120	21.60	406	Feb 2004*	0.34	0.01
<i>K</i>	CFHT	21590	3255	23.70	413	Mar 2007	0.34	0.01
<i>IRAC1</i>	Spitzer	35635	7430	23.90	413	Jan 2006	0.34	0.01
<i>IRAC2</i>	Spitzer	45110	10110	23.30	413	Jan 2006	0.33	0.01
<i>IRAC3</i>	Spitzer	57593	14060	21.30	413	Jan 2006	0.33	0.01
<i>IRAC4</i>	Spitzer	79594	28760	21.00	413	Jan 2006	0.32	0.01
<i>MIPS24</i>	Spitzer	236741	50560	80 μ Jy	385	Jan 2006-Jan 2008		
<i>MIPS70</i>	Spitzer	714329	184844	4 mJy	34	Jan 2006-Jan 2008		
<i>MIPS160</i>	Spitzer	1558938	344982	30 mJy	8	Jan 2006-Jan 2008		
<i>L</i>	VLA	1.4GHz	75MHz	45 μ Jy	139 ⁸	Aug 2003-Mar 2006		

¹ Effective wavelength: $\lambda_{eff} = \int R * \lambda d\lambda / \int R d\lambda$, where R is the transmission profile normalized to a peak throughput of unity, and including the transmission of the atmosphere, the telescope, the camera optics, the filter and the detector.

² The FWHM of the response function.

³ 5σ in a $3''$ aperture for data from infrared to UV bands. Flux limit for the radio and X-ray (in $\text{erg cm}^{-2} \text{s}^{-1}$) data.

⁴ k_λ is the constant parameter for each band to calculate the Galactic extinction by $A_\lambda = k_\lambda E(B-V)$.

⁵ Galactic extinction calculated by k_λ in each band multiplied by mean $E(B-V)$ 0.0192 (see § 4.1.1).

⁶ The rest of the sources are so bright that they saturate in the band.

⁷ The rest are out of the region of the Hubble coverage.

⁸ 61 sources have $> 5\sigma$ detections, 78 sources have $3\sigma \sim 5\sigma$ detections. In addition, 268 other sources have 3σ upper limits.

* These photometry data were excluded after variability correction.

** The unit is $\text{erg}/(\text{cm}^2\text{s})$.

(0.5 – 2 keV) and $\sim 3 \times 10^{-15} \text{ erg cm}^{-2}\text{s}^{-1}$ (2 – 10 keV) over 90% of the surveyed area. As such XMM-COSMOS is the deepest survey over such a large contiguous solid angle (2.13 deg^2) performed to date with XMM-Newton (Cappelluti et al. 2009). X-ray fluxes were computed from the count rates assuming the Galactic column density of $N_H = 2.6 \times 10^{20} \text{ cm}^{-2}$ (Dickey & Lockman 1990), and spectral indices of $\Gamma = 2$ for the 0.5 – 2 keV band, and $\Gamma = 1.7$ for the 2 – 10 keV band (Cappelluti et al. 2009). A total of 1848 point-like sources were detected:

1567 in the 0.5 – 2 keV, 1096 in the 2 – 8 keV band, and 245 in the 4.5 – 10 keV band, excluding those associated with extended X-ray sources.

Brusa et al. (2007, 2010) used the likelihood ratio technique (Sutherland & Saunders 1992, Ciliegi et al. 2003, Brusa et al. 2005, Civano et al. 2012) to identify the counterparts of XMM-COSMOS sources using the optical (CFHT I band), near-infrared (CFHT K band) and mid-infrared (IRAC) catalogs. For the subfield of the XMMCOSMOS covered also by Chandra, the opti-

cal identifications have been augmented with the more accurate Chandra positions (Civano et al. 2012). 85% (1577) of the *XMM-Newton* sources have a unique and secure optical counterpart with a probability of misidentification of < 0.01 (i.e. no ambiguous optical counterparts, no *XMM-Newton* sources separated into two sources in the *Chandra* catalog, see Table 1 of Brusa et al. 2010 for details.). The counterparts have been cross-correlated with the full COSMOS photometric catalog (Capak et al. 2007), including optical bands from CFHT, SDSS and Subaru multiwavelength bands (Taniguchi et al. 2007), which consists of 6 broad ($\Delta\lambda = 800\text{--}1500 \text{ \AA}$) bands, 12 intermediate ($\Delta\lambda = 300\text{--}500 \text{ \AA}$) bands and 2 narrow ($\Delta\lambda = 150\text{--}200 \text{ \AA}$) bands. The counterparts have also been cross-correlated with the CFHT J-band (Ilbert et al. 2009), CFHT K-band (Mc Cracken et al. 2010) catalog. The sources were also associated with *GALEX* sources from the deblended, PSF-fitted *GALEX* COSMOS catalog (Zamojski et al 2007), and with the IRAC (Sanders et al. 2007), the MIPS $24\mu\text{m}$ (Le Floch et al. 2009), and the $70\mu\text{m}$ (Frayser et al. 2009, Kartaltepe et al. 2010) catalogs. More details on cross-correlation procedure and source identification are available in Brusa et al. (2010).

The counterpart positions were then cross-correlated with all the available redshift catalogs in the field, including the most recent SDSS release (Schneider et al. 2007), the COSMOS AGN spectroscopic survey and the zCOSMOS survey catalogs. The Magellan/IMACS AGN spectroscopic survey has optical spectra of an X-ray and optical flux-limited sample (down to $f_{0.5\text{--}10 \text{ keV}} > 8 \times 10^{-16} \text{ erg cm}^{-2}\text{s}^{-1}$ and $i_{AB}^+ < 23$) of 677 *XMM-Newton* selected sources over the entire COSMOS field. Trump et al. (2009a) find 485 high-confidence redshifts from the first 3 years of the Magellan/IMACS survey, with a total of 588 AGN with high-confidence redshifts at the survey’s completion. zCOSMOS is a redshift survey of 20,000 galaxies in the COSMOS field taken with the VLT/VIMOS spectrograph. The zCOSMOS bright sample is magnitude-limited with $i_{AB}^+ < 22.5$. *XMM-Newton* source counterparts were targeted explicitly. About 500 *XMM-Newton* sources have zCOSMOS spectra (many of which also have IMACS spectra). In summary, a total of 886 unique good quality spectroscopic redshifts are available, or $\sim 50\%$ of the entire XMM-COSMOS sample (see details in Brusa et al. 2010). From this sample, we selected all the objects identified as type 1 AGN (i.e. those showing broad emission lines with $\text{FWHM} > 2000 \text{ km s}^{-1}$ in their optical spectra). This gives the final sample of 413 type 1 XMM-COSMOS AGN: the “XC413” sample.

The near-infrared data set of COSMOS so far has only the J and K bands, leading to rather sparse coverage of the rest frame optical parts of the SEDs for redshifts $\sim 1\text{--}2$. H-band imaging of the COSMOS field to $H_{AB} \sim 21$ has been obtained as part of the Heidelberg InfraRed/Optical Cluster Survey (HIROCS survey; Falter et al. 2004). H-band total magnitudes (obtained through PSF fitting) for 218 type 1 AGN in this sample were supplied to us (H.-J. Röser, private communication).

1.4 GHz counterparts to the X-ray sources were determined by positional matching the optical coordinates of the X-ray sources to the positions in the VLA-COSMOS

Joint catalog (Schinnerer et al. 2010) with a search radius of $1''$. The VLA-COSMOS joint catalog lists 2900 sources detected at $S/N \geq 5$ in the COSMOS field. All successful matches (61 sources) were unique. The AIPS/MAXFIT peak finding algorithm was used to search for additional radio detections within a $2.5'' \times 2.5''$ box centered on the optical coordinates of unmatched X-ray sources. For the 78 detections in the range $3\text{--}5 \sigma$, we computed their total flux using the assumption that they are not resolved at 1.4GHz (beam FWHM $2.5''$). For flux peaks with a lower significance level we derived a 3σ upper limit based on the local rms noise (calculated within a $17.5'' \times 17.5''$ box) at the position of the radio source.

To derive SEDs for the XC413, we made use of all the data described above. Overall, the photometry is complete in 30 bands for more than $\sim 99\%$ of the XC413 sample, and it is complete in 5 additional bands for more than $\sim 90\%$ of the sample. In the infrared to ultraviolet wavelength range, where the bulk of the AGN power is radiated, we have complete coverage in the 6 infrared bands (IRAC 1–4, J and K), and complete, richer, coverage in the optical (Subaru broad and intermediate bands). This makes the XC413 sample the best so far with which to study the infrared to optical SED in great detail. Table 1 reports the bands used, their effective wavelengths and filter widths, the limiting depth of the survey, the number of XC413 sources having a detection in each band, and the observation dates. For convenience we also tabulate the value of A_λ for the typical Galactic extinction and the coefficient, k_λ , used for each band to calculate the Galactic extinction.

3. SAMPLE PROPERTIES

The depth of the multi-wavelength coverage in COSMOS results in a wide range of detectable fluxes at most wavelengths. In Figure 1, we show the COSMOS “spectral window function” (Brissenden 1989) over the infrared to ultraviolet bands of XC413 in $\log \nu f_\nu$ versus $\log \nu$ space. The spectral window function is composed of two curves: the upper one picks out the brightest objects in the XC413 sample in each band; the lower one shows the limiting flux for detection in each band. The spectral window function thus shows the range of SEDs detectable for a sample. The width of the window function in the X-ray band is also indicated with arrows on the right. The XC413 AGN spectral window function has a typical width of ~ 3 dex in the infrared–optical–ultraviolet part of the spectrum where the bulk of the AGN power is radiated. This is about twice the range in the E94 sample (dashed blue lines) in almost all of the bands. Hence, the XC413 sample is capable of revealing a larger variety of type 1 AGN SEDs than the E94 sample (see § 4.5 for details).

3.1. Luminosity and Redshift

In Figure 2, 3 and 4 the properties of the XC413 sample (black crosses) are compared to the E94 quasars (magenta squares).

Figure 2 shows the rest frame 2 keV X-ray luminosity versus redshift plane. For the XC413 quasars (black crosses), the 2 keV luminosity is calculated from the observed X-ray band flux and the spectral index Γ (Mainieri

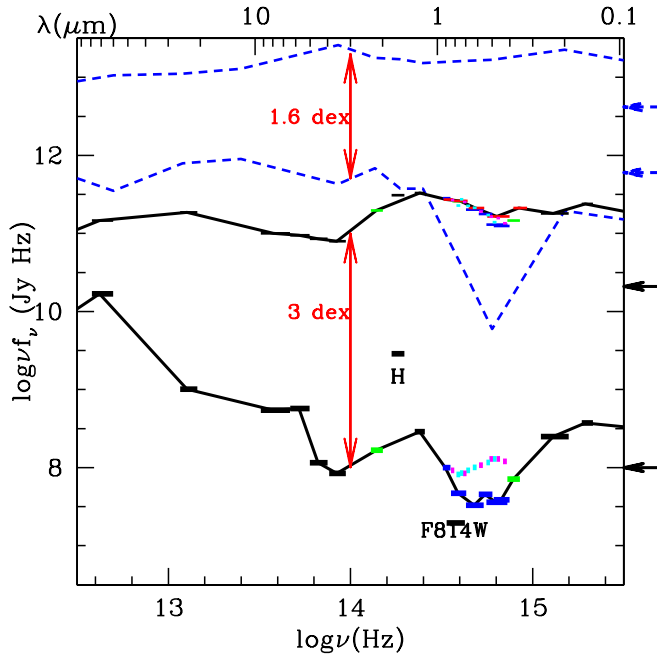


FIG. 1.— Spectral window function of the 413 type 1 AGN in XMM-COSMOS (XC413, black solid line) compared to the E94 (blue dashed line) sample. The spectral window function consists of two lines. The upper line shows the brightest data and the lower line shows the limits of each band. From the left to right the points are: MIPS70, MIPS24, IRAC4 to IRAC1 (black), CFHT K band (green), H band (black), J band (black), ACS F814W band (black), Subaru broad bands (blue), SDSS (red), Subaru intermediate bands (2006 magenta, 2007 cyan), CFHT u band (green), GALEX NUV and FUV bands (black). The X-ray window width at 2 keV is shown as arrows on the right.

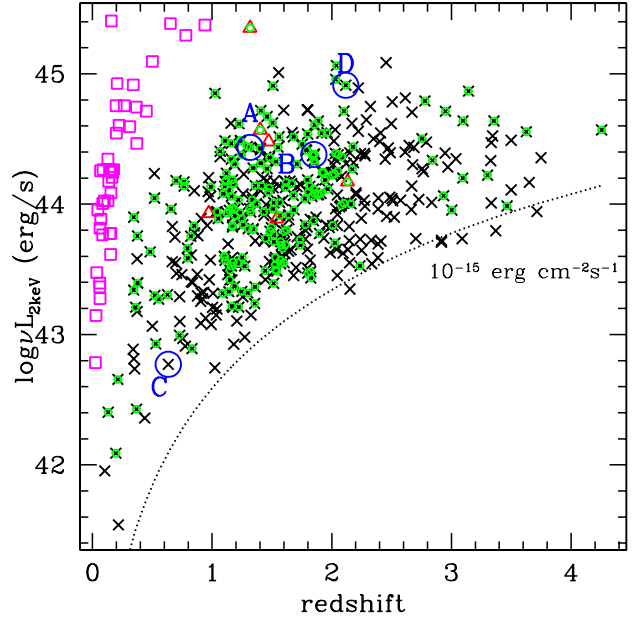


FIG. 2.— X-ray luminosity versus redshift for the 413 type 1 AGN in XMM-COSMOS. The depth of the survey is $\sim 5 \times 10^{-16} \text{ erg cm}^{-2} \text{ s}^{-1}$ (0.5–2 keV) and $\sim 3 \times 10^{-15} \text{ erg cm}^{-2} \text{ s}^{-1}$ (2–10 keV) over 90% of the area. The dotted line shows the X-ray flux of $10^{-15} \text{ erg cm}^{-2} \text{ s}^{-1}$ as a guidance of the flux limit. Quasars from E94 are shown as magenta squares. Black crosses = radio quiet sources, red triangles = radio loud sources (see § 3.3 for the definition). Green hexagons = sources corrected for host galaxy contribution (see § 4.4). The four sources labeled (A, B, C, D) in blue are discussed in § 4.5.

et al. 2007). For the XC413 quasars without Γ estimation, spectral index $\Gamma = 2$ for the 0.5–2 keV band and $\Gamma = 1.7$ for the 2–10 keV band is assumed (Cappelluti et al. 2009). The magenta squares represent the 47 E94 quasars in the same plot. The 1 keV monochromatic luminosity and the spectral index α_x for each E94 quasar respectively (E94 Table 2) has been used to calculate the 2 keV monochromatic luminosity of the E94 sample. Notice that E94 uses $H_0 = 50 \text{ km s}^{-1} \text{ Mpc}^{-1}$, so we computed the X-ray luminosity with the same cosmology used in this paper.

In Figure 3, we show the *i* band absolute magnitude M_i – redshift plane. For E94 we derived *i* band magnitudes using the *V* band magnitude and (B–V), (R–I) colors from E94 (Table 4A), and the transformation from the Johnson system to the AB magnitude in *i* band given by Jester et al. (2005, Table 1; $r - i = 0.90(R - I) - 0.20$ and $r = V - 0.19(B - V) - 0.02$). Note that we first recalculated the tabulated E94 M_V with the same cosmology used in this paper. In Figure 4, we show the location of the XC413 sample with respect to the E94 sample in the *i* band absolute magnitude M_i versus X-ray luminosity plane. We can clearly see that the XC413 sample covers a larger luminosity and redshift range compared to the E94 sample.

The XC413 sample is ten times larger than the E94 quasar sample. Over two orders of magnitude range in luminosity, the XC413 sample homogeneously covers a redshift range (80% quasars at $0.1 \leq z \lesssim 2.2$) ~ 6 times larger than the E94 sample (80% quasars at $z < 0.35$),

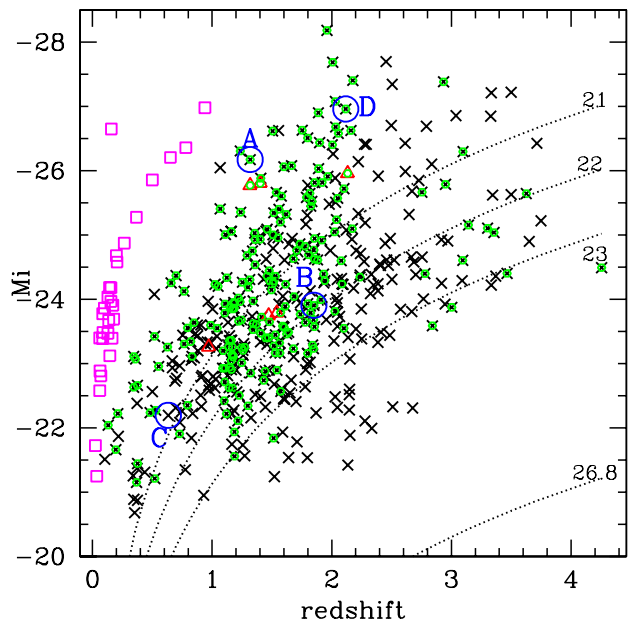


FIG. 3.— *i* band absolute magnitude versus redshift for the 413 type 1 AGN in XMM-COSMOS. The dotted lines represent the SDSS photometry flux limit ($i=21$ mag), the Magellan and MMT flux limit ($i=23$ mag) and the photometry flux limit ($r=26.8$ mag). The symbols are as in Figure 2.

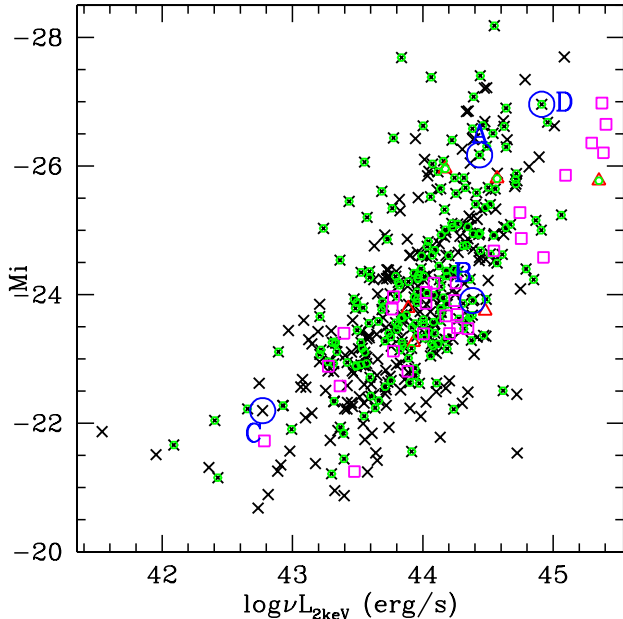


FIG. 4.— I band absolute magnitude versus X-ray luminosity for the 413 type 1 AGN in XMM-COSMOS. The symbols are as in Figure 2.

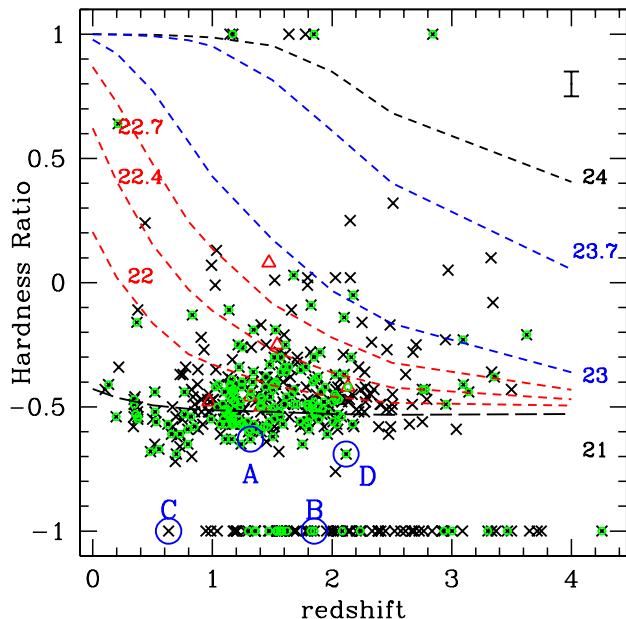


FIG. 5.— Hardness ratio $((H-S)/(H+S))$ versus redshift for the XC413 sample. The symbols are the same as in Figure 2. The lines show the tracks for different column density labeled in $\log(N_H)$. The line in the upper right corner showed the size of the mean error bar of HR.

and a flux range some 2 dex fainter than the E94 sample ($16.9 \leq i_{AB} \leq 24.8$). While the two samples span comparable range of M_i , the COSMOS sample includes many more lower luminosity ($\log \nu L_{2keV} < 10^{43.5} \text{ erg/s}$) X-ray sources compared to E94 sample (see Figure 2).

3.2. X-ray Properties

The hardness ratios of the XC413 AGN are shown versus redshift in Figure 5. The hardness ratio is defined as $HR=(H-S)/(H+S)$, where H are the counts in the 2-10 keV band and S those in the 0.5-2 keV soft energy band (Brusa et al. 2010). Usually, a negative HR indicates the absence of X-ray absorption, although for a given spectrum the HR is a strong function of redshift. There are 73 (17.6%) quasars with $HR=-1$, which is reasonable fraction for type 1 AGNs (e.g. Rosati et al. 2002). There are also 6 quasars with $HR=1$ in XC413, which is somewhat unexpected. We will discuss the properties of these 6 quasars in a following paper. Figure 5 also shows the curves of hardness ratio versus redshift for a range of equivalent hydrogen column densities (N_H), computed using XSPEC (version 11, Arnaud 1996), assuming a spectral slope of $\Gamma = 1.7$ and solar abundances. Most(299) of the XC413 AGN have HR values indicative of small absorbing hydrogen column densities, $N_H < 10^{22} \text{ cm}^{-2}$, as is typical of most type 1 AGN (e.g., Mainieri et al. 2007). However, 27.6% (114) of the XC413 sample shows HR indicative of obscuration $N_H > 10^{22} \text{ cm}^{-2}$ and even larger. Mainieri et al. (2007) estimated the N_H value for 378 quasars of the XC413 from the X-ray spectrum. Only 36 out of the 378 quasars have N_H value larger than 10^{22} cm^{-2} . For the 114 quasars lie above the $N_H = 10^{22} \text{ cm}^{-2}$ curve in the HR versus redshift plane, 19 quasars have estimated $N_H > 10^{22} \text{ cm}^{-2}$, 76 quasars have estimated $N_H < 10^{22} \text{ cm}^{-2}$ and 19 quasars without the N_H estimation from the X-ray spectrum. From the Figure 5, we can also see that majority of the sources above the $N_H = 10^{22} \text{ cm}^{-2}$ curve cluster near the curve within the range of the typical HR error bar. A similar results have been found by Lanzuisi et al. (2012) for the bright sources in the C-COSMOS survey (Elvis et al. 2009).

A deeper analysis of the X-ray properties of this sample, including the optical to X-ray slope analysis, has been reported in Lusso et al. (2010) and Brusa et al. (2010).

3.3. Radio Loudness

Quasars are often classified into radio-loud and radio-quiet, based on their radio properties. Typically, 10% of all quasars are radio-loud (e.g. Kellermann et al. 1989; Urry & Padovani 1995; Ivezić et al. 2002).

There are several ways to classify quasars as radio-loud or radio-quiet. We tried: (1) $R_L = \log(f_{5GHz}/f_B)$ in the rest frame (Wilkes & Elvis 1987, Kellermann et al. 1989), for which $R_L > 1$ defines a radio loud source; (2) $q_{24} = \log(f_{24\mu m}/f_{1.4GHz})$ in the rest frame and observed frame (Appleton et al. 2004), for which $q_{24} < 0$ is defined as radio-loud; (3) $R_{1.4} = \log(f_{1.4GHz}/f_K)$ in the observed frame, for which $R_{1.4} > 1$ defines a radio loud source; (4) $R_{uv} = \log(f_{5GHz}/f_{2500\text{\AA}})$ in the rest frame (e.g., Stocke et al. 1992; Jiang et al. 2007), for which $R_{uv} > 1$ defines a radio loud source; (5) $\log_{10}[P_{5GHz}(W/H z/Sr)] > 24$ in the rest frame (Goldschmidt et al. 1999) as radio-loud; (6) $R_X = \log(\nu L_\nu(5GHz)/L_X) > -3$ in the rest frame (Terashima & Wilson 2003) as radio loud.

After cross-checking with all the above criteria, there are 6 sources classified as radio-loud in all cases³¹. We define these 6 of the 413 sources as radio-loud sources.

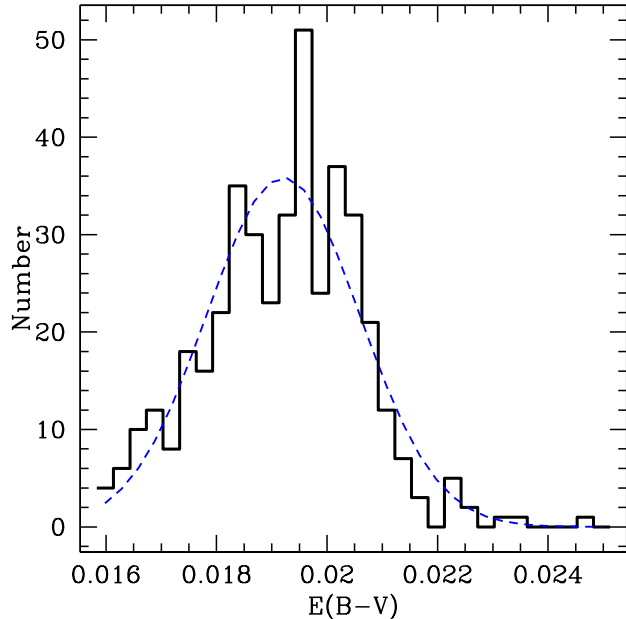


FIG. 6.— Distribution of estimated Galactic extinction for the XC413 AGN. Blue dashed line = Gaussian fit.

For the most commonly used criteria, using the R_L criterion, there are 17 radio-loud quasars. Using the q_{24} criterion, there are 13 radio-loud quasars. Using both R_L and q_{24} criteria, gives 8 radio-loud sources³³. The fraction of radio-loud sources in the XC413 sample is no more than 4.5% using any one criterion, and no more than 2.1% using two or more criteria, smaller than the $\sim 10\%$ seen in typical optically selected AGN samples (e.g. Peterson et al. 1997). The VLA detection is deep enough that for great majority of the quasar in XC413 (95.7%) the VLA data would detect a radio-loud quasar, using any standard criteria. The radio-loudness of the XC413 sample and the effects of the detection limits in radio to this fraction will be discussed in a later paper (Hao et al. 2012c, Paper IV).

4. SPECTRAL ENERGY DISTRIBUTIONS

Our goal is to produce uniform rest frame SEDs for all the XC413 quasars. To do so, several corrections to the observed SEDs need to be considered. The corrected SEDs can then be converted to a uniform grid in the rest frame to calculate the mean and dispersion.

4.1. Corrections to the Observed SEDs

Several complicating factors need to be considered before we can study the SED of the individual sources: (1) Galactic extinction, (2) variability, (3) emission line flux contamination; (4) host galaxy contamination. In this subsection, we will discuss the first three effects, deferring the host galaxy correction, which is more complex and requires more assumptions, to §4.4.

4.1.1. Galactic Extinction

³² XID=40, 2282, 5230, 5275, 5517, 5395.

³⁴ The two additional sources using R_L and q_{24} criteria are XID=5497, 54541.

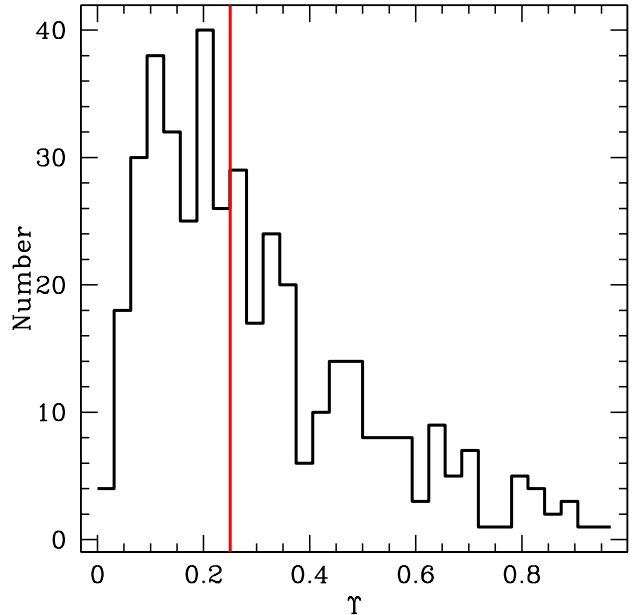


FIG. 7.— Distribution of the variability parameter Υ (Salvato et al. 2009) of the XC413 AGN. The vertical line divides the sources into variable (>0.25) and not-variable (<0.25).

Although the Galactic extinction is small in the COSMOS field, with a median of $E(B-V) = 0.0195$ (Capak et al. 2007), we include the correction on a source-by-source basis to eliminate this factor. A photometric correction for each band of the source is calculated from the Galactic extinction of this source multiplied by the filter-dependent factor k given in Table 1. The factors are calculated by integrating the filter response function against the Galactic extinction curve from Cardelli et al. (1989).

The estimated $E(B-V)$ from Schlegel et al (1998) for the XC413 AGN has a mean of 0.0192 and a standard deviation of 0.0014. For the most affected band – the FUV band, the mean Galactic extinction is $\sim 0.17 \pm 0.01$ mag, which reduces to 0.10 ± 0.03 mag for the shortest wavelength optical band (the CFHT u-band). A histogram of $E(B-V)$ for the sample is shown in Figure 6.

4.1.2. Variability

The COSMOS optical and infrared data were taken over a 4 year interval, from 2004 to 2007, and the SDSS data for the field were taken as early as 2001. This long time span causes problems in deriving the true shape of the SEDs, because AGN are significantly variable on these timescales (Hawkins 2007, Sergeev et al. 2006). Most AGN vary in their optical continuum flux on the order of 10% on timescales of months to years (Vanden Berk et al. 2004).

Variability is common in the XC413 sample too. Salvato et al. (2009) analyzed the variability of all the XMM-COSMOS X-ray sample and defined a convenient variability parameter Υ (the rms of the magnitude offsets at the sampled epochs) to quantify the variability of the sources. Salvato et al. (2009) found that $\Upsilon > 0.25$ efficiently separates out variable XMM-COSMOS sources (including both point-like and extended sources). Half of the XC413 AGN show significant variability by this

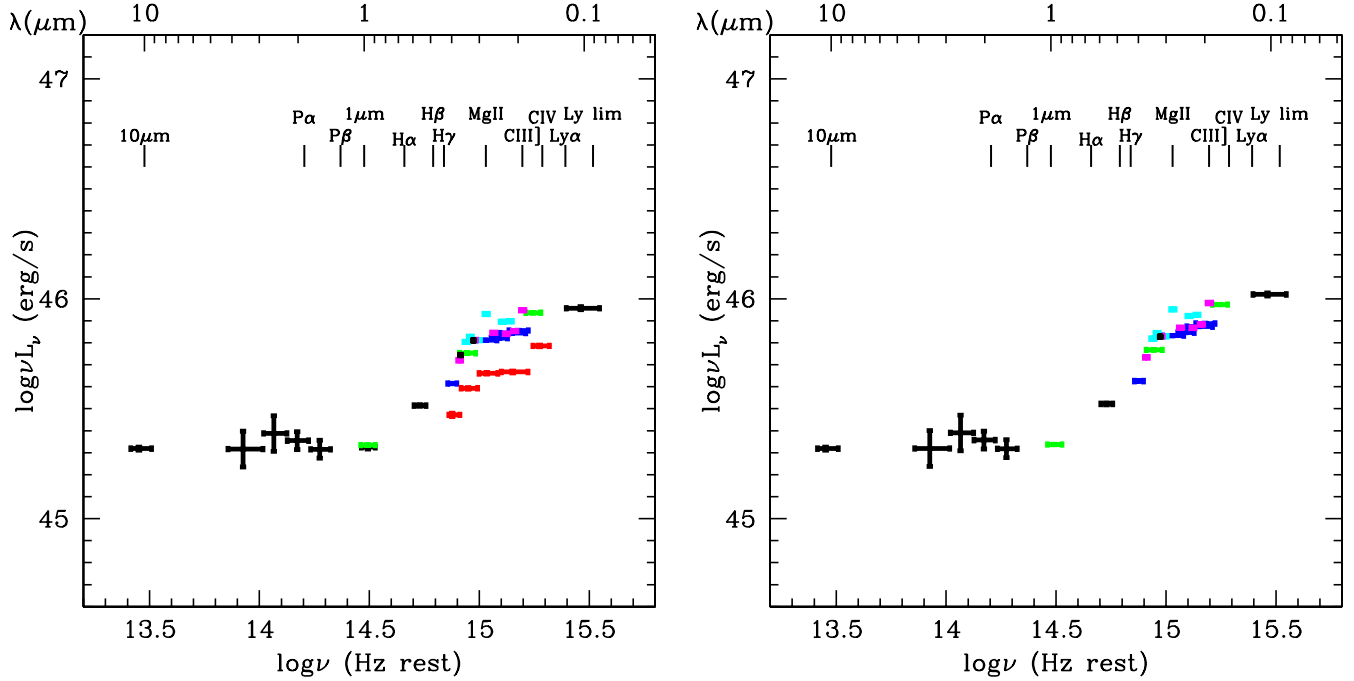


FIG. 8.— Type 1 AGN SED showing clear flux and slope variability in the optical/UV. The source is COSMOS_J149.85194+1.99845 (XID=17) at $z=1.236$, (i -band absolute magnitude -26.3). *Left*: SED resulting from using all the data (2001-2007). *Right*: only the data in the years 2004-2007. The data points are: black, from low frequency to high frequency, are: $24\mu\text{m}$, $8\mu\text{m}$, $5.7\mu\text{m}$, $4.5\mu\text{m}$ and $3.6\mu\text{m}$, K-band, H-band, J-band and the FUV and NUV. The red points show the broad SDSS ugriz bands from 2001. The blue points are the Subaru broad bands from 2005. The green points are the (CFHT) K-band, and the (CFHT) u band and i band. The purple points are the 6 Subaru intermediate bands for season 1 (2006) (IA427, IA464, IA505, IA574, IA709, IA827). The cyan points are the 5 Subaru intermediate bands for season 2 (2007) (IA484, IA527, IA624, IA679, IA738, IA767).

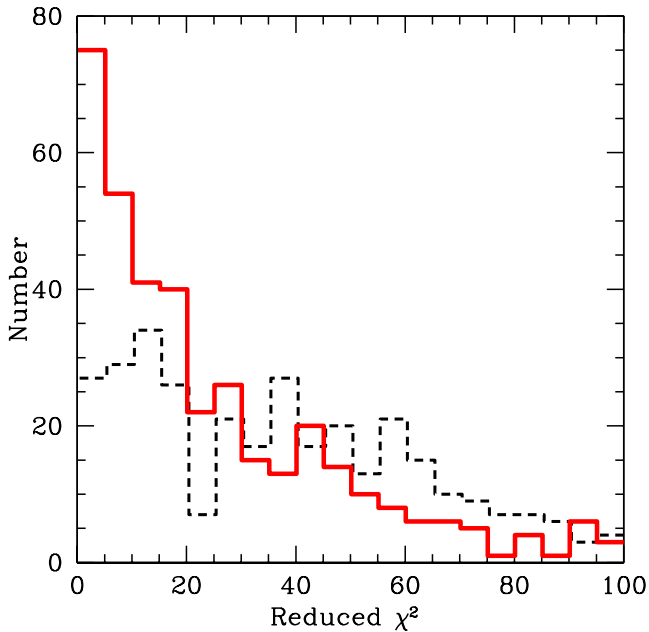


FIG. 9.— The reduced χ^2 of the SED-fitting (see §4.2.2) both before (black) and after (red) the restriction of the data to the 2004-2007 interval.

criterion (Figure 7).

An example of an AGN SED from this sample (XID=17), that clearly changes both in flux and in optical/UV slope, is presented in Figure 8 (left). The resulting SED is confused when the entire time period is

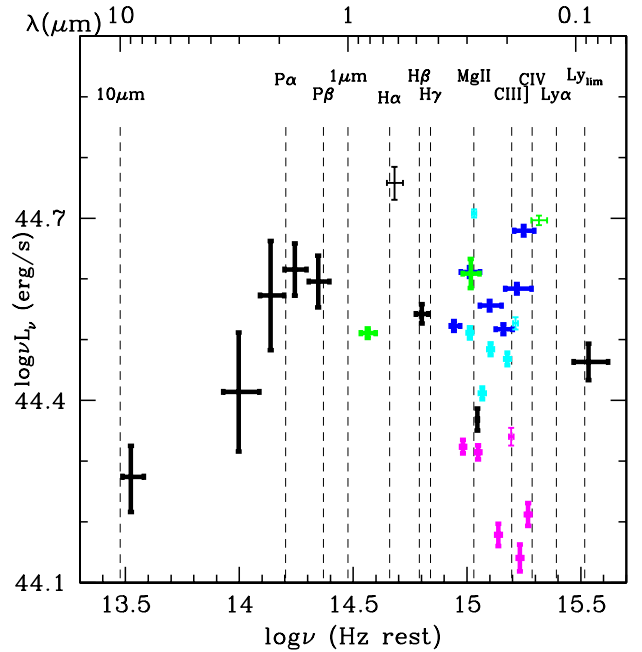


FIG. 10.— SED (restricted 2004-2007 interval) of source COSMOS_J150.48437+2.16204 (XID=2232) at $z=1.641$ (i -band absolute magnitude -23.5). The inconsistent photometry, notably in the UV, suggests more rapid variability in this object, and in the 5% of similar sources, than is typical of the majority of the population. The points are color coded as in Figure 8.

included. This is a widespread problem. Figure 9 shows the broad χ^2 distribution obtained in fitting a quadratic function to the SEDs of the full data set. Details of the

SED fitting used here will be discussed in §4.2.2.

We do not use the Salvato et al. (2009) method to correct the SED, although it works well for deriving photometric redshifts. This is because the method introduces an assumed smooth average SED shape to estimate the correction to be made to each photometry band for variability. This might bias estimates of the intrinsic SED shape.

The alternative approach which we adopt is simply to restrict the data set to a shorter time period. For this approach, we experimented with several different temporal cuts, trying to find the best compromise between contemporaneity and completeness of coverage. Using χ^2 fits to the continuum, we find that by using only the data in the interval from 2004 to 2007 reduces the variability issue. Beyond that, we exclude the K band from KPNO because it duplicates the K band from CFHT, which is deeper and has better photometry. We also exclude the data in the filter NB816 because the photometry in this band is the sum of runs distant in time and is thus not reliable due to the variability of the quasars.

Figure 8 (bottom) shows how using only the 2004-2007 data removes the scatter in the same AGN (XID=17) shown in Figure 8 (top). Similar improvements are common. The solid line in Figure 9 shows how the reduced time span greatly improves χ^2 (with a distinct peak at low χ^2) after applying these restrictions. The peak reduced χ^2 is still ~ 5 , which is mainly due to two reasons: 1) the photometry of the data is so good that deviations from the simple assumed continuum, due e.g. to weak emission lines and blends, as well as weak residual variability, remain significant; 2) when calculating the χ^2 , we use the formal photometric errors from various catalogs, which are usually somewhat underestimated.

The SEDs of $\sim 5\%$ of the sources remain scattered, as in the example in Figure 10. While some of the points are strongly affected by emission lines (see next section), even the unaffected points seem to show ~ 0.3 dex changes. This indicates more rapid variability than is seen in the majority of the sample.

The 8 photometric bands excluded are starred in Table 1. We have 35 photometry bands remaining with high photometry quality. This temporal cut gives a sample free of strong variability without having to make any assumptions for the SED shape, and retaining virtually the same photometric coverage.

4.1.3. Broad Emission Line Fluxes

The broad emission lines (BELs) of quasars clearly affect the photometry in numerous objects. Figure 11 shows an example, in which the broad Ly α emission line has increased the intermediate band by ~ 0.3 dex compared to the adjacent broad band. Similarly, the broad C IV emission line has increased the flux by approximately 0.1 dex. Visual inspection shows that 280 of the 413 AGN have photometry that appears clearly affected by BELs.

To correct the SEDs for BEL contamination, we need to measure or estimate equivalent widths (EWs) for all the strong BELs in the quasar spectra. Although, by construction, we have optical spectra for each of the type 1 AGN in the sample, these spectra do not span the full spectral range required. Typically only one or two BELs

are present in each optical spectrum. Estimates of EW for most of the BELs are still needed.

For the BELs in the spectra of IMACS/Magellan, VIMOS/VLT or SDSS (Trump et al. 2007, 2009a; Lilly et al. 2007, 2009; Schneider et al. 2007), the EWs were measured individually using the `splot` package in IRAF³⁵. The number of measured EWs for the major BELs are shown in the second column of Table 2. The MgII BEL has measured EWs for 33% of the sample (137/413), but no other BEL has more than 17% coverage.

For the remaining BELs, we must estimate their EWs by other means. We considered three methods:

1. Use correlations of EW between the different BELs to bootstrap from the observed lines to the rest;
2. Use the known relationships between CIV EW and luminosity or redshift, i.e. the Baldwin effect (Baldwin 1977), or analogs for other lines (Green et al. 2001).
3. Take a mean or median EW for each BEL from a survey covering a wide redshift range, in order to cover all the major BELs, and use the dispersion of the observed EW as an error bar on the estimate.

(1) *BEL correlations.* This method leads to large uncertainties on the BEL EW estimates. We studied the correlation between the EWs of the main BELs using the complete, UV-excess selected, Palomar-Green X-ray sample with redshift $z < 0.4$ (Shang et al. 2007). We found that some line pairs had well-correlated EWs: MgII and CIV (correlation coefficient, $R = 0.93$), Ly α and CIV ($R = 0.86$), CIII] and CIV ($R = 0.90$), CIII] and MgII ($R = 0.82$), H α and H β ($R = 0.91$). However, there was either no or weak correlation between some other key line pairs: the Balmer lines with MgII, CIV, CIII], or Ly α , and Ly α with MgII ($R < 0.5$). This is quite a surprising result, and may indicate a wider variety of ionizing continua and/or BLR conditions and geometry than has been typically considered (Ferland and Osterbrock 2005). In order to eliminate the effect of different selection methods, we also studied the correlation between BELs for an X-ray selected survey, the RIXOS survey (Puchnarewicz et al. 1997). We found no strong correlation between *any* of the BELs ($R < 0.4$) in the RIXOS survey.

(2) The *Baldwin effect and its analogs* can be studied using EWs from the Large Bright Quasar Survey (LBQS) sample (Green et al. 2001). Green et al. (2001, Figures 1, 4) show that the widths of the correlations between BEL EW and either monochromatic luminosity at 2500 Å or redshift is ~ 1 dex, too large to provide useful EW estimates.

(3) The *EW mean and dispersion for each BEL*, require a large sample to give well-determined values. The obvious choice is the SDSS spectroscopic sample of quasars. We used the EWs of the seven main BELs and the narrow [O III] doublet (Table 2) from SDSS DR7 (Abazajian

³⁵ IRAF is distributed by the National Optical Astronomy Observatory, which is operated by the Association of Universities for Research in Astronomy, Inc., under cooperative agreement with the National Science Foundation.

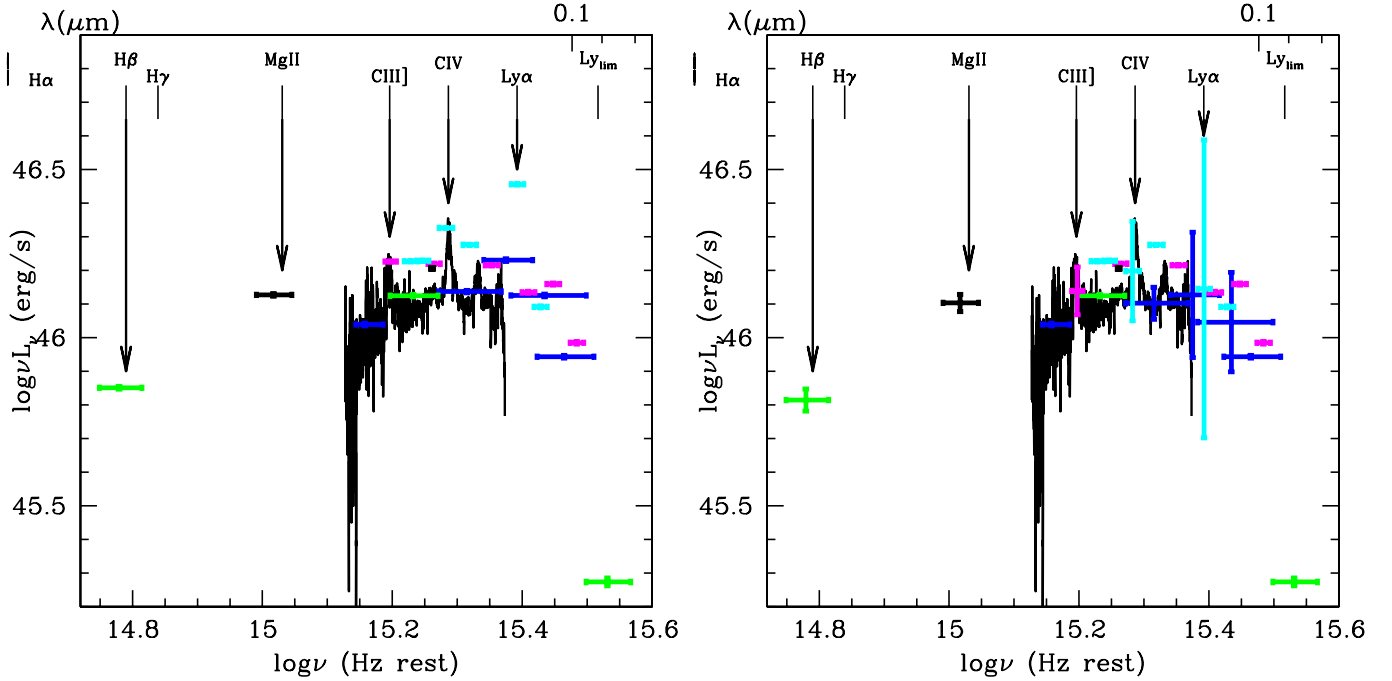


FIG. 11.— *Left*: Optical SED of COSMOS_J150.20885+2.481935 (XID=180) at $z=3.333$ (i band absolute magnitude -27.19), strongly affected by BELs. Highly significant departures due to $\text{Ly}\alpha$ and C IV distort fits to the continuum SED by ~ 0.3 dex and ~ 0.1 dex, and possible BELs of C III], Mg II and $\text{H}\beta$ are also apparent. The black solid line show the VLT spectrum of this source. *Right*: Optical SED of COSMOS_J150.20885+2.481935 (XID=180) after removing the emission lines using the prescription in §4.1.3. The error bars on the affected photometry points become larger because of the wide spread in BEL EWs (Figure 12). The black solid line show the VLT spectrum of this source. The points are color coded as in Figure 8.

TABLE 2
SPECTRAL LINE REST-FRAME EQUIVALENT WIDTH FROM SDSS DR7

Spectral Line	N^1	Mean 2 (Gaussian) EW(Å)	Mean 3 (Log Normal) EW(Å)	σ^3 (Log Normal) EW(Å)	correction 4 r (dex)	correction 5 IA624 (dex)
$\text{Ly}\alpha$	4	55.3	58.6	50.5	0.052	0.200
C IV	39	26.3	26.7	15.2	0.024	0.103
C III]	70	17.6	17.6	6.7	0.016	0.070
Mg II	137	20.8	20.7	8.4	0.019	0.082
$\text{H}\gamma$	21	13.4	13.5	6.1	0.013	0.055
$\text{H}\beta$	25	29.3	29.8	17.4	0.027	0.113
[O III]4960	19	13.7	12.4	10.4	0.012	0.051
[O III]5008	19	25.0	22.3	22.5	0.021	0.087
$\text{H}\alpha$	13	204.3	186.7	226.0	0.148	0.457

¹ This column is the number of detections in our optical (Magellan/MMT/SDSS) spectra for each spectral line.

² Mean EW correspond to the Gaussian fit of the histogram in Figure 12.

³ The mean and sigma of the log-normal fit of the histogram in Figure 12.

⁴ Typical correction for a broad band for quasars at redshift $z = 2$, here we use r band ($\text{BW}=1382\text{\AA}$) as an example. The correction is calculated as $\log(\text{BW}/(\text{BW} + \text{EW}_{rest} * (1 + z)))$.

⁵ Typical correction for an intermediate band for quasars at redshift $z = 2$, here we use IA624 ($\text{BW}=300\text{\AA}$) as an example. The correction is calculated as $\log(\text{BW}/(\text{BW} + \text{EW}_{rest} * (1 + z)))$.

et al. 2009), as retrieved from the SDSS archive³⁷. We do not directly use the composite quasar spectrum from SDSS (Vanden Berk et al. 2001), because the EW distribution dispersion for each BEL is not available.

For each quasar, we used only those lines for which the DR7 indicated a good fit ($n\text{sigma} > 10$), which amounts to about 65% of the SDSS type 1 AGN. As the cataloged EW are in the observed frame, we transformed them to

the rest frame by dividing them by the $(1 + z)$, where z is the corresponding redshift of the SDSS quasar. Figure 12 shows the resulting distributions of the rest-frame equivalent width of the emission lines we consider sorted in wavelength. A Gaussian is a reasonably good approximation for the $\text{Ly}\alpha$, and to a lesser extent, $\text{H}\beta$ and $\text{H}\gamma$ distributions. However, C IV, C III], Mg II, [O III], and $\text{H}\alpha$ show quite skewed distributions, with a tail to large EW, so that a Gaussian is a poor approximation. For these lines we instead fit a log-normal distribution to the his-

³⁸ <http://www.sdss.org/dr7/products/spectra/index.html>

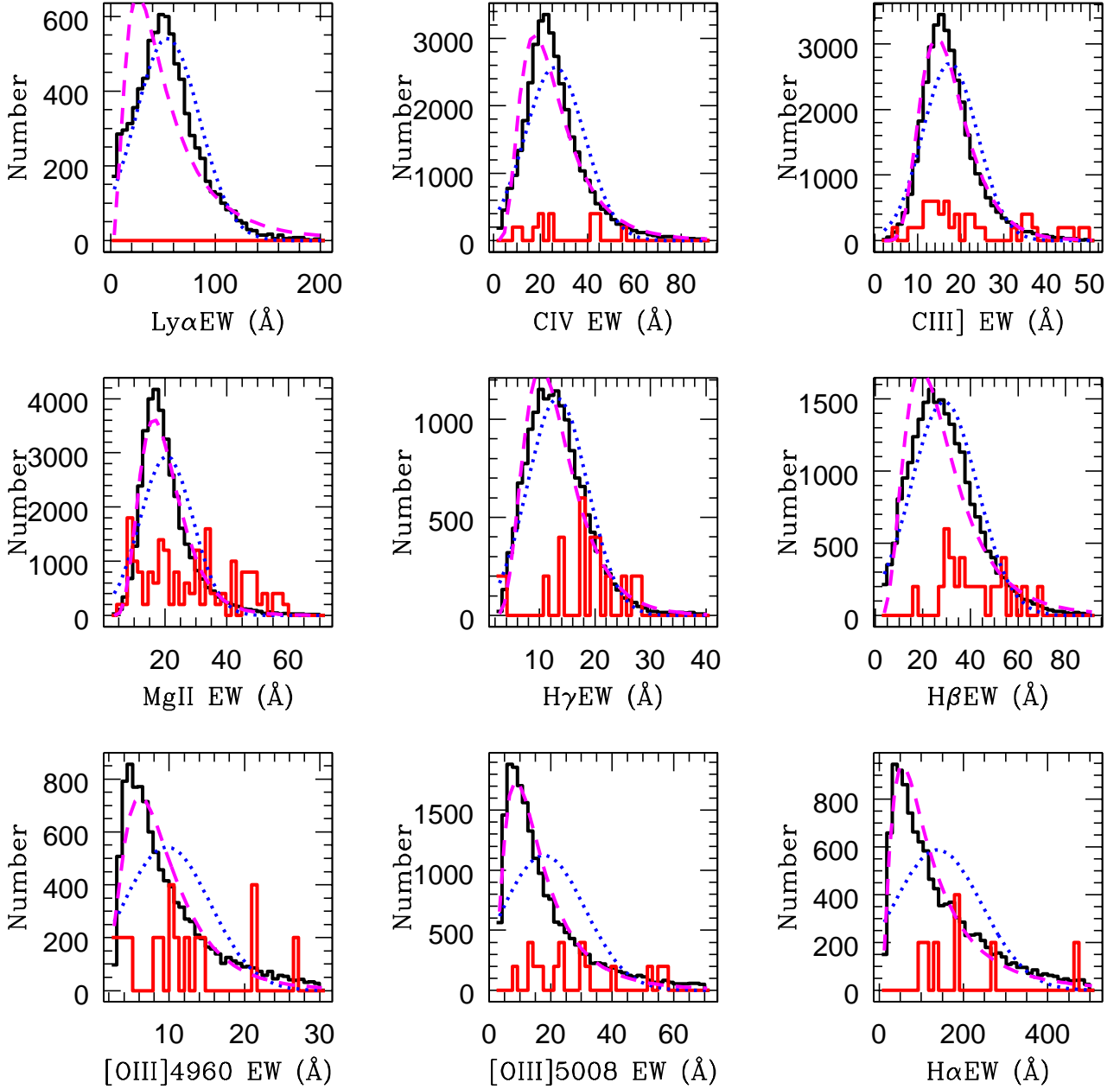


FIG. 12.— EW distributions of 7 BELs and the [OIII] doublet from SDSS DR7 (black histogram). Blue dotted line = Gaussian fit; magenta dashed line = log-normal fit. The EWs measured for the COSMOS Type 1 AGN sample is shown as a red solid histogram, multiplied by 200 for plotting purposes. For $\text{Ly}\alpha$, the 4 measured EWs are all larger than the range of the histogram.

tograms. This produced much better fits (Figure 12). The resulting mean and sigma of the log-normal distribution are given in Table 2.

Comparing these three methods, we find that the mean and dispersion of the EW from SDSS provides the best correction.

We adopted the mean and sigma from Table 2 as the mean rest-frame EW and the error bar in making the BEL subtraction from the SEDs. We made the following simplifying assumption to calculate the BEL correction:

when the BEL central wavelength lies within the photometry band, which is equivalent to having more than 1/2 the BEL flux in the filter assuming symmetry, we consider them as if the entire line profile were in the range. When the central BEL wavelength is outside the filter band, we assume the contribution of the broad emission line is negligible.

We need to transform the rest-frame EW back to the observed EW of the quasar in XMM-COSMOS sample $EW_{obs} = EW_{rest} \times (1 + z)$. Here z is the redshift of the

quasar undergoing the correction. The EW uncertainties were added to the photometric errors according to the formula below.

Assuming that the continuum flux f_c is constant across each broad band photometry interval, then the integrated total flux (νf_ν) in the broad band photometry range is F_O . If the bandwidth is BW, it is easy to see that $F_O = f_c \times EW_{obs} + f_c \times BW$, based on the definition of EW. The integrated continuum flux can then be calculated as,

$$F_c = f_c \times BW = \frac{F_O * BW}{EW_{obs} + BW} = \frac{F_O \times BW}{EW_{rest} \times (1 + z) + BW} \quad (1)$$

so the correction that needs to be applied to the $\log \nu f_\nu - \log \nu$ diagram is $\log(BW/(EW_{obs} + BW)) = \log(BW/(EW_{rest} \times (1 + z) + BW))$. The error on the integrated continuum flux is

$$\begin{aligned} d(\log \nu f_\nu) &= d(\log \nu f_O) + d(EW_{obs})/(EW_{obs} + BW) \\ &= d(\log \nu f_O) + \frac{d(EW_{rest})(1 + z)}{EW_{rest} \times (1 + z) + BW} \quad (2) \end{aligned}$$

As can be seen from the above formula, the correction for the BEL emission is, naturally, larger if the bandwidth is smaller. For broad band photometry, the filter width is of order $\sim 1000 \text{ \AA}$, while the observed EW of the BELs is of order $\sim 100 \text{ \AA}$ for the strongest lines, leading to a $\sim 10\%$ correction to the measurement of the continuum, according to equation (1). Assuming the error of the measurement of the observed EW is the square root of the measurement ($\sim 10 \text{ \AA}$), the error caused by the correction is then $\sim 1\%$, according to equation (2). The Subaru intermediate bands have filter widths of $\sim 200 \text{ \AA}$ (Table 1), so the correction for these bands is ~ 3 times larger. To illustrate how large the correction is, the corresponding corrections for an intermediate band (IA624) and broad band (r band) are shown in Table 2. Note that no H α line would lie in these two bands.

As a final step we checked that the correction was reasonable by visual inspection. We find that 217 of the 286 AGN with clear BEL contributions appear to be well-corrected by the scheme adopted, while 21 appear over-corrected and 48 still appear to have residual BEL emission in their SEDs. The error bars at the positions of the excised BELs are large in the corrected SEDs, due to the additional correction error, which means these affected bands will weigh less in the SED fitting.

Note that previous SED studies (e.g., E94, Richards et al. 2006) do not include the BEL corrections as we did here, because the SEDs in those studies were all constructed using broad band photometry, which is affected only at the 1%–5% dex level by the BEL contribution (Table 2, column 6). For H α , which would only be found in the i band and beyond (typically J H or K bands), the effect will be less than 7% dex. Instead in COSMOS, the majority of the optical SED comes from the Subaru intermediate bands (season 1 and 2, 12 bands), which are affected by the BEL contribution at 5% to 20% dex level (Table 2 last column). To minimize the confusion to the SED shape from the intermediate bands by this effect, the BEL correction is thus necessary for XC413 sample.

4.2. Conversion to a Uniform Rest Frame Grid

The redshifts of the sample quasars range from 0.1 to 4.3, so any observed photometry point spans a wide range of rest frame frequency. To study the individual SEDs, and to calculate a mean SED, we clearly need to shift the SEDs of the quasars to a common rest frame frequency grid. For ease of comparison to E94, we adopted the grid of the E94 mean SED, which has points separated by 0.02 in logarithmic frequency.

We first converted the flux densities at each frequency for each object to luminosity, and shifted the observed frequencies to the rest frame for each source. We then tried two techniques for interpolating the observed photometry to the uniform grid points: linear interpolation and polynomial fitting. Both methods have advantages and disadvantages. In section 4.3, we will see that the resulting mean SED using both methods agree well with each other with difference less than 0.02 dex in rest frame 0.1–10 μm (Figure 15). The wavelength/frequency discussed in this section are all in rest frame.

4.2.1. Linear Interpolation

The simplest way to produce a uniformly sampled SED is to linearly interpolate between the data points in $\log \nu L_\nu$ versus $\log \nu$ space (i.e. connecting the individual points with a power law in linear space).

The COSMOS photometry for the XC413 sample is $>90\%$ complete from u (CFHT) to MIPS $24\mu\text{m}$ (Table 1). The apparent drop in the i band from Subaru is due to saturation; the remaining objects are picked up in the i (CFHT) data. The H-band (Calar Alto) is only 61% complete, but the neighboring J, K data is complete making interpolation straightforward. So over the 1.8 dex wide $0.35\mu\text{m} - 24\mu\text{m}$ ($\sim 0.14\text{mum} - 10\mu\text{m}$ for the typical $z = 1.5$ of XC413) observed frame interpolation is unproblematic.

For the mid-infrared part of the SED the $70\mu\text{m}$ and especially the $160\mu\text{m}$ detections become sparse (8% and 2% respectively). For the detections we joined the $24\mu\text{m}$ data to the longer wavelength points with a power-law in $\log \nu f_\nu$ vs. $\log \nu$ space. For non-detections we extrapolated from the rest frame $24\mu\text{m}$ to $8\mu\text{m}$ slope. We checked if the extrapolation generally works by checking the SEDs of the 34 quasars with MIPS70 detection (3 of them also have MIPS160 detection). We found that only for 17.6% quasars (6 out of 34), the extrapolation of the $24\mu\text{m}$ to $8\mu\text{m}$ exceed the observations. For half of the 6 quasars, the deviation is within 1σ , which means the extrapolation only fails in 8.8% of the case. So we use this extrapolation for all the XC413 quasars without $70\mu\text{m}$ and $160\mu\text{m}$ detections.

In the sub-mm/mm band from 100 GHz (3 mm) to $160\mu\text{m}$ part, the SED can be approximated by the red end of the grey body $f_\nu \propto \nu^{3+\beta} / (e^{h\nu/kT} - 1)$, when $h\nu \ll kT$, $f_\nu \propto \nu^{2+\beta}$ (e.g. Lapi et al. 2011). β is generally chosen in the range 1–2 (Dunne & Eales 2001), and we used $\beta = 1$. I.e. we assume a power-law $f_\nu \propto \nu^3$ in this band.

For the radio band, for each source with a $> 3\sigma$ detection, we assumed a power law $f_\nu \propto \nu^{-0.5}$ (e.g., Ivezić 2004) in the rest frame 1.4 GHz (21 cm) to 100 GHz (3 mm) range. The radio power is never a significant contributor to the total luminosity ($<3\%$ Hao et al. 2012a). For sources with only a radio upper limit, we extend the

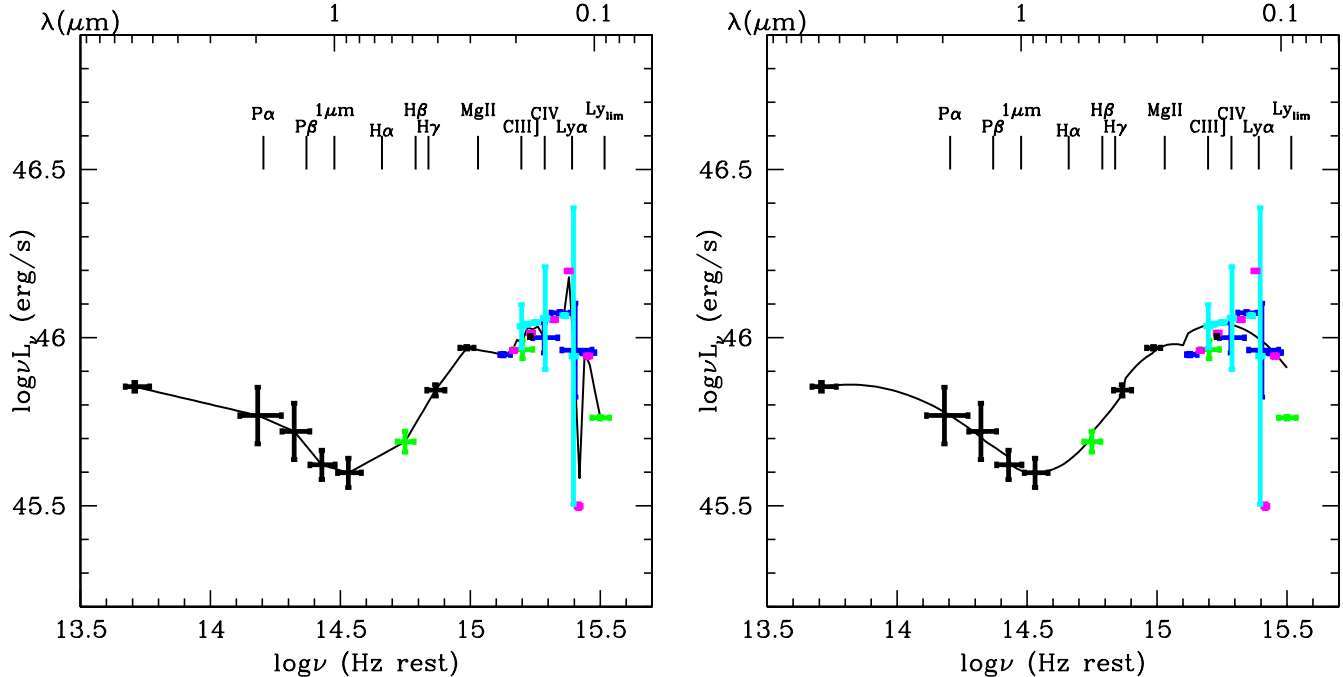


FIG. 13.— *Left*: SED of COSMOS_J150.6088+2.76966 (XID=5331) at $z=3.038$, with i band absolute magnitude -26.84 , after the broad emission line and variability (by restricting the dates of the data set) corrections. The black line shows a linear interpolation through the corrected data set. *Right*: SED of COSMOS_J150.6088+2.76966 (XID 5331). The black line shows the quadratic fit to the corrected data set. The reduced χ^2 is 145.1. The points are color-coded as in Figure 8.

power-law of $f_\nu \propto \nu^3$ in the sub-mm/mm to the radio wavelength.

Turning to the high frequency SED: The bluest band in the optical with complete coverage is the u band at $0.38 \mu\text{m}$. In the ultraviolet the COSMOS photometric completeness drops to 60% at $0.23 \mu\text{m}$ (GALEX NUV) and 33% at $0.15 \mu\text{m}$ (GALEX FUV). The FUV points would add little to the SED study as FUV fluxes are strongly reduced by the Lyman- α forest induced break at $0.12 \mu\text{m}$ for $z \gtrsim 0.3$, i.e. the great majority of the sample (408/413=99%). The Lyman- α forest affects the NUV photometry for $z > 0.9$ (358/413=87% of XC413). Almost all (146/150) the quasars without NUV detection are at $z > 0.9$ and all the quasars without FUV detection are at $z \gtrsim 0.3$.

For the X-ray band, we used the photon spectral index (Γ) for the 318 objects in Mainieri et al (2007). For the remainder we assumed flat X-ray spectrum $\Gamma=2$ (Cappelluti et al. 2009). The observed 0.5 keV–10 keV fluxes correspond to a rest-frame band of 1.25 keV–25 keV at $z = 1.5$. We thus extrapolated the observed flux to get the luminosity in the rest-frame 0.5 keV–40 keV band using the power law slope $2 - \Gamma$ in the $\log \nu f_\nu$ versus $\log \nu$ space.

To join the soft X-rays to the UV through the unobservable EUV band we directly connect the detections in the optical or uv to the 0.5 keV flux with a power-law in $\log \nu f_\nu$ versus $\log \nu$ space in keeping with the findings of Laor et al. (1997).

Although linear interpolation is simple, this method could be inappropriate for several reasons:

1. The optical data are rich, and overlapping of bands occurs frequently in this range. The data were taken over a 4 year time interval, so that fluxes in adjacent and overlapping bands can be discon-

tinuous;

2. The EW correction for the BELs is not perfect, which could drag the ‘continuum’ to deviate from the correct value;
3. The fluxes in different filters have different error bars and so should be weighted differently, which cannot be done by interpolation.

These factors can lead to poor continuum fits when a linear interpolation is used, and also does not make use of the information contained in the error bars.

4.2.2. Polynomial Fitting

An alternative to the linear interpolation is to make a weighted fit of the data using a low order polynomial. We tried several curve fitting methods and found that a simple least squares quadratic fit works well.

For each source, we fit quadratic functions to the observed data from rest frame 9000 \AA to the Lyman limit (912 \AA). The longer wavelength data ($1\text{--}160 \mu\text{m}$) were interpolated with a second quadratic function. We smooth the junction of the two quadratics by quadratic interpolation with a smoothing window of 10 grid points, corresponding to a factor of 1.6 in frequency. The disadvantage of this fitting method is that a particular functional form is assumed, which may not be a good representation of the true SED shape of the AGN. Just over 50% of the sources gave reduced $\chi^2 < 20$, showing that additional structure, or residual variability, is likely to be present. An example of the linear integration and the quadratic fit is shown in Figure 13. For this quasar, the reduced $\chi^2 = 145.1$.

The resulting SEDs for each of the objects in the XC413 are available as VO compatible FITS files in the on-line version of the paper.

4.3. Full Sample Mean SED and Dispersion

The Galactic extinction, variability and emission line corrections done in the previous sections are based on reasonable assumptions without a strong model dependency. We can check the mean and dispersion of the SEDs after these corrections.

We used both the linearly interpolated SEDs and the SED fitting to calculate the mean and dispersion of the sample SEDs. We calculated the arithmetic mean of the $\log\nu L_\nu$ at each frequency of the grid. As described above, in the rest frame infrared to ultraviolet range, both methods are based only on detection (see details in § 4.2.1).

The mean SED of the XC413 AGN, after applying all the above corrections, is shown in Figure 14 (left) as a black solid line, as well as the E94 mean radio-quiet and radio-loud SEDs (red and green dashed line, respectively). For comparison, we also plot the mean SED normalized at $1\mu\text{m}$, as for the E94 mean SEDs, (Figure 14 right), to avoid a bias towards high luminosity sources. The XC413 mean SED is definitely flatter at all wavelengths than both E94 SEDs.

Three galaxy templates from SWIRE³⁹ (Polletta et al. 2007) are also shown in the same plot (Figure 14): a spiral galaxy (Spi4), an elliptical galaxy with an age of 5 Gyr, and a starburst galaxy (NGC6090). These templates are normalized to the value of $\log L_K^* = 44.32$ ($M_K^* = -23$) from the UKIDSS Ultra Deep Survey (Cirasuolo et al. 2007). The XC413 mean SED could be flat because affected by contamination from a strong host galaxy component.

We compare the infrared to ultraviolet mean SED before and after the corrections for Galactic reddening, variability and BEL EW on a much expanded scale in Figure 15. The differences are strongly correlated with the location of the BELs, meaning that that the BEL has been properly corrected in at least 8 out of 9 (90%) lines. Even though the EW distribution (Figure 12) does not show a peculiar behavior, the CIV emission line correction, as derived from SDSS, is not sufficient in our sample (~ 0.02 dex higher than continuum). The polynomial fit makes the SED shape smoother compared to linear interpolation, however the difference between the two methods is less than 0.02 dex in the 0.1–1 μm range.

Concentrating on the UV to IR (0.1–10 μm) range, it is clear from Figure 14 that the mean SED of the XC413 sample is quite flat, and lacks the clear $1\mu\text{m}$ inflection point between the UV and near-IR bumps seen in E94. E94 found that host galaxy corrections were significant even in the most luminous quasars in their sample⁴¹.

³⁹ The 16 galaxy templates in the “SWIRE Template Library” (Polletta et al. 2007) include: 3 elliptical galaxy templates “Ell2”, “Ell5”, “Ell13” representing elliptical galaxy of age 2 Gyr, 5 Gyr and 13 Gyr respectively; 7 spiral galaxy templates “S0”, “Sa”, “Sb”, “Sc”, “Sd”, “Sdm”, “Spi4”; and 6 starburst galaxy templates “NGC6090”, “M82”, “Arp220”, “IRAS20551-4250”, “IRAS22491-1808”, “NGC6240”.

⁴¹ In retrospect, this result, like those of McLeod et al. (1994) and Eskridge et al. (1995), was an early hint of the correlation between host bulge mass and central black hole mass (Magorrian et al. 1998).

The dispersion of the SEDs, computed using the median SED and the 68, 90 and 100 percentile contours on each side of the median are shown in Figure 16, together with the E94 SED. The upper 90th percentile SED shows a E94 like shape, while the lower 90th percentile SED is close to the galaxy templates shown in Figure 16. Typically X-ray selected AGN samples, such as XMM-COSMOS, include more sources with low AGN to host galaxy contrast, compared to optically selected samples, and so are more affected by the host galaxy contribution. Due to the bias of the optical color selection, optically selected samples tend to select sources with clear big blue bumps, thus missing the many quasars with large host contributions (compare to Richards et al. 2006 and Luo et al. 2010).

4.4. Host Galaxy Correction

Jahnke et al. (in prep.) uses the COSMOS high-resolution HST/ACS F814W image (Koekemoer et al. 2007) to estimate the host galaxy luminosity and AGN luminosity for XMM-COSMOS sources at $z < 1$. We could use their results by normalizing a galaxy template to the galaxy luminosity at the observed frequency and subtracting the galaxy contribution from the observed SED. However, this method does not work well for our sample, for the following reasons:

1. We have to assume the host galaxy type in which the AGN is harbored. The F814W band would be at $\sim 3000\text{\AA}$ rest frame for a typical XC413 quasar at redshift $z = 1.5$, which lies on the steeply falling blue side of the galaxy template, so that a small error in template slope (or, effectively, in the age of the youngest population in the host) would lead to a large error in the normalization (Figure 17). In the XMM-COSMOS sample, this issue leads to a severe over-subtraction problem in some cases. For a 5 Gyr old elliptical galaxy template, 9 out of the 89 sources with host magnitude estimation are over-subtracted (10%). For spirals and starburst galaxies, this method completely fails, as the over-subtraction fraction is $>80\%$.
2. Direct imaging works only for the 89 sources at low redshift ($z < 1$) for which the HST F814W image gives a good host galaxy magnitude estimates (Jahnke et al. in prep.). For the remaining 324 sources in the sample, we cannot perform a host galaxy correction with this method.

Estimates of host luminosity have been made using other techniques:

(1) Vanden Berk et al. (2006) use the eigenspectrum decomposition technique to give a host to AGN relationship in r band, which can be transformed to luminosity as follows (Richards et al. 2006, hereinafter R06).

$$\log(L_{r,Gal}) = 0.87\log(L_{r,AGN}) + 2.887 - \log\lambda_E \quad (3)$$

where λ_E is the Eddington ratio.

(2) Marconi & Hunt (2003) analyze two-dimensional images of nearby galaxies with a black hole mass determined with direct gas kinematics or stellar dynamics (Tremaine et al. 2002) in the local universe. Their results

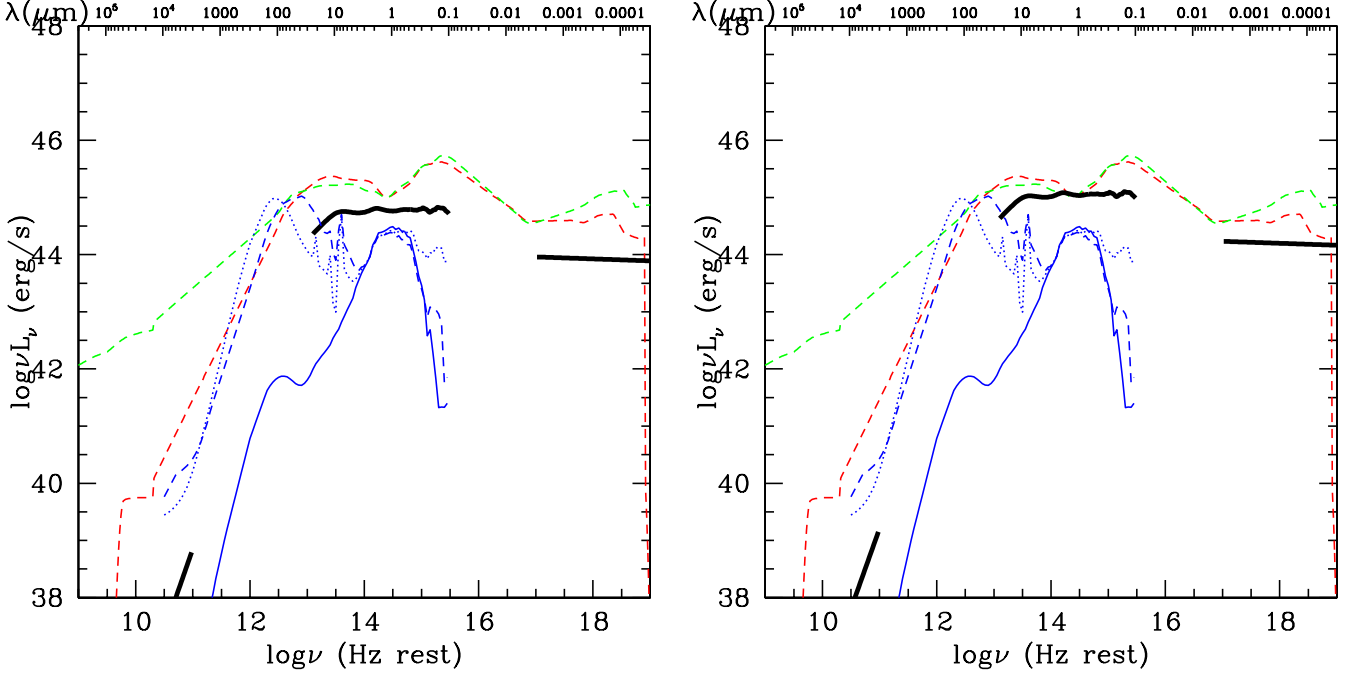


FIG. 14.— The mean SED for all the quasars in XC413 after the Galactic extinction correction, variability constraints, and broad emission line correction (black solid line): *Left*: arithmetic mean of the $\log \nu L_\nu$; *Right*: arithmetic mean of the $\log \nu L_\nu$ after normalization at $1\mu\text{m}$. The dashed lines are the mean radio-loud (green) and radio-quiet (red) SEDs from E94. The blue lines show galaxy templates from Polletta et al. (2007), normalized to the UKIDSS L_K^* value; blue solid line = elliptical galaxy with 5 Gyr of age (Ell5), blue dotted line = Spiral galaxy (Spi4), blue dashed line = a starburst galaxy (NGC6090).

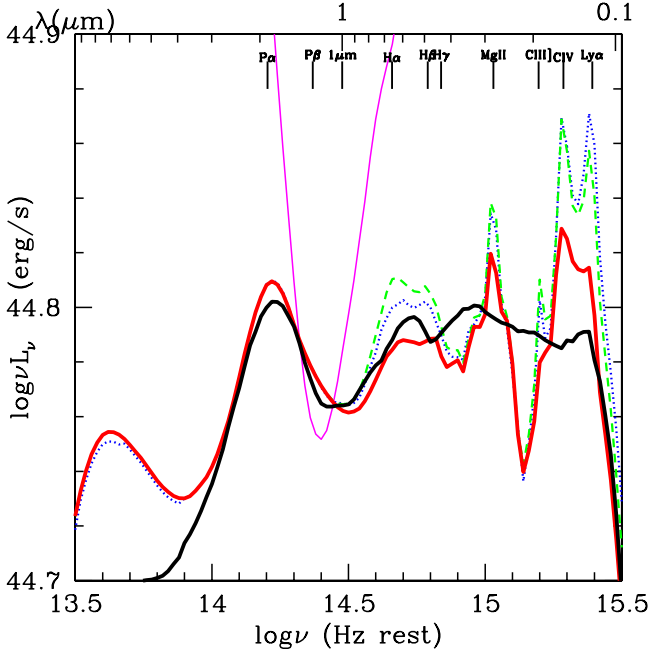


FIG. 15.— Comparison of the mean IR to UV XC413 SED derived by different methods. (Note that the y-axis has a much expanded scale compared with Figure 13). Blue dotted line = ‘raw’ mean SED before corrections; green dashed line = mean SED after the Galactic extinction correction and variability restriction. The two solid lines are the mean SEDs after the Galactic extinction correction, variability restriction and BEL EW correction: red line = mean SED by linear interpolation; black line = mean SED by polynomial fitting. The E94 radio quiet mean SED is shown in magenta solid line.

can be transformed as below:

$$\log(L_{B,Gal}) = 0.84 \log(L_{bol}) + 3.914 - 0.84 \log \lambda_E \quad (4)$$

$$\log(L_{J,Gal}) = 0.88 \log(L_{bol}) + 3.545 - 0.88 \log \lambda_E \quad (5)$$

$$\log(L_{H,Gal}) = 0.86 \log(L_{bol}) + 4.530 - 0.86 \log \lambda_E \quad (6)$$

$$\log(L_{K,Gal}) = 0.88 \log(L_{bol}) + 3.577 - 0.88 \log \lambda_E \quad (7)$$

The above relation is derived for the local universe. However there is evidence that the black hole mass and host luminosity relationship evolves with redshift (Peng et al. 2006a,b; Ho 2007; Decarli et al. 2010; Merloni et al. 2010; Bennert et al. 2010, 2011). Allowing for selection effects, the evolutionary trend is $M_{BH}/L_{sph} \propto (1+z)^{1.4 \pm 0.2}$ (Bennert et al. 2010, 2011). As most XC413 quasars are at high redshift, we need to include this effect. We added an additional redshift term in the above equations (4–7), giving the following equations:

$$\log(L_{B,Gal}) = 0.84 \log(L_{bol}) + 3.914 - 0.84 \log \lambda_E - 1.18 \log(1+z) \quad (8)$$

$$\log(L_{J,Gal}) = 0.88 \log(L_{bol}) + 3.545 - 0.88 \log \lambda_E - 1.23 \log(1+z) \quad (9)$$

$$\log(L_{H,Gal}) = 0.86 \log(L_{bol}) + 4.530 - 0.86 \log \lambda_E - 1.20 \log(1+z) \quad (10)$$

$$\log(L_{K,Gal}) = 0.88 \log(L_{bol}) + 3.577 - 0.88 \log \lambda_E - 1.23 \log(1+z) \quad (11)$$

We choose the rest frame J band luminosity $L_{J,gal}$, because this is the band closest to $1\mu\text{m}$, where the galaxy contributes strongly. The rest frame J band is also located on the flat part of the host templates, so the

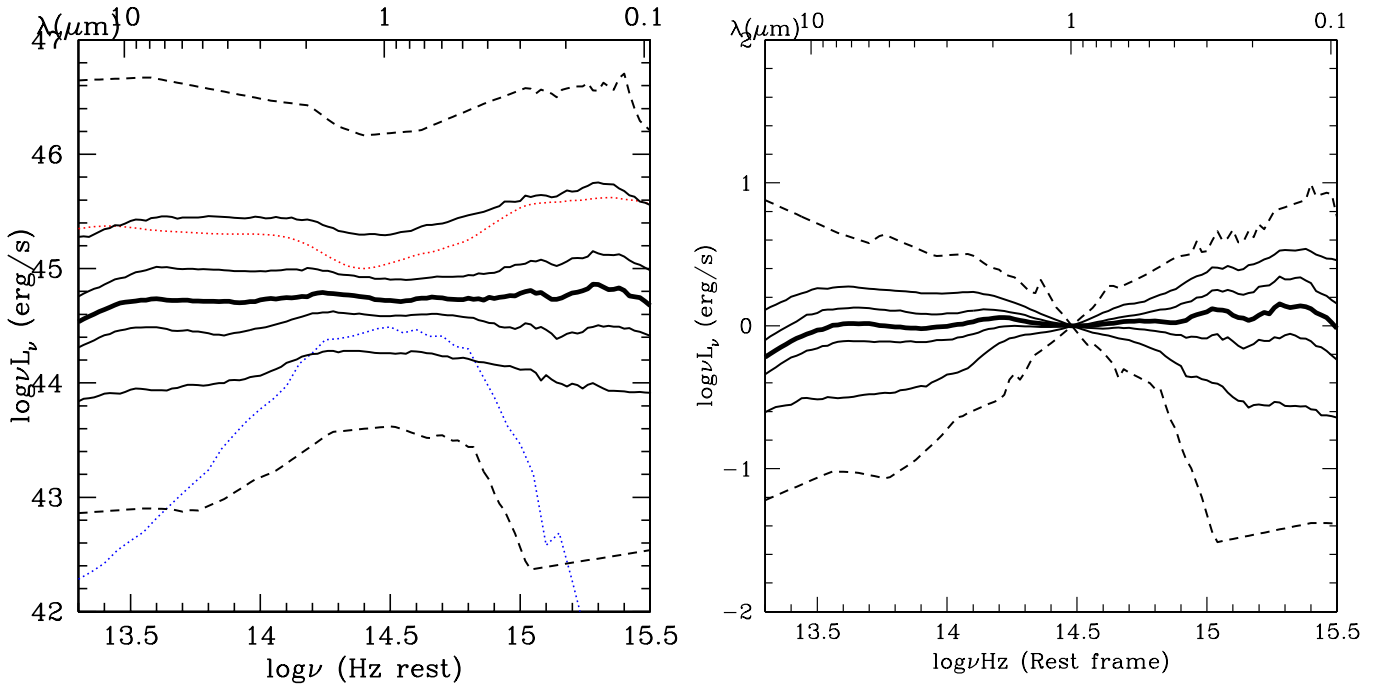


FIG. 16.— The pre-host subtraction median (thick black line) SED and the 68%, 90% (thin solid black lines) and 100% (dashed black lines) percentile envelopes in the ultraviolet to infrared ($0.09\mu\text{m}$ - $24\mu\text{m}$) range: *Left*: without normalization; *Right*: normalized at $1\mu\text{m}$. Red dotted line= E94 RQ mean SED. Blue dotted line=5 Gyr elliptical galaxy template (Ell5).

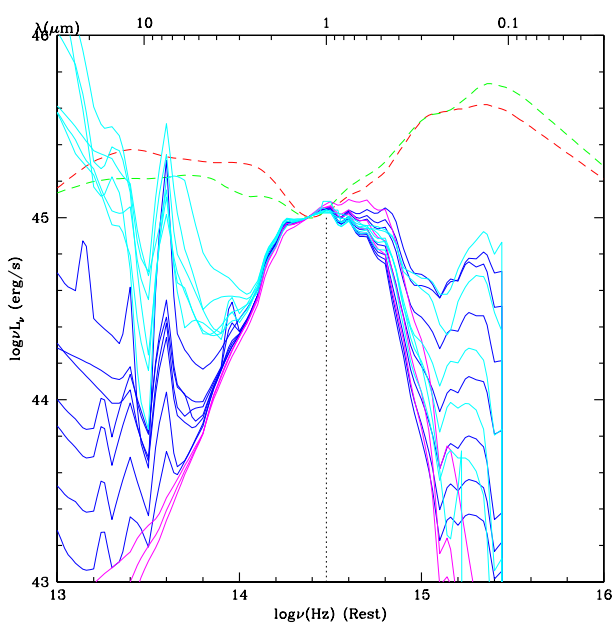


FIG. 17.— SED of 16 galaxy template from SWIRE template library (Polletta et al. 2007) normalized at rest frame J band are shown as solid line (blue=spiral galaxy: S0, Sa, Sb, Sc, Sd, Sdm and Spi4; magenta=elliptical galaxy with 2 Gyr, 5 Gyr and 13 Gyr of age; and cyan=starburst galaxy: NGC6090, M82, Arp220, IRAS20551-4250, IRAS22491-1808, NGC6240). The E94 mean SED are shown as dashed lines (red as radio quiet and green as radio loud).

normalization is insensitive to uncertainties in the template slope, in contrast to the observed F814W band for quasars at redshift 1–2.

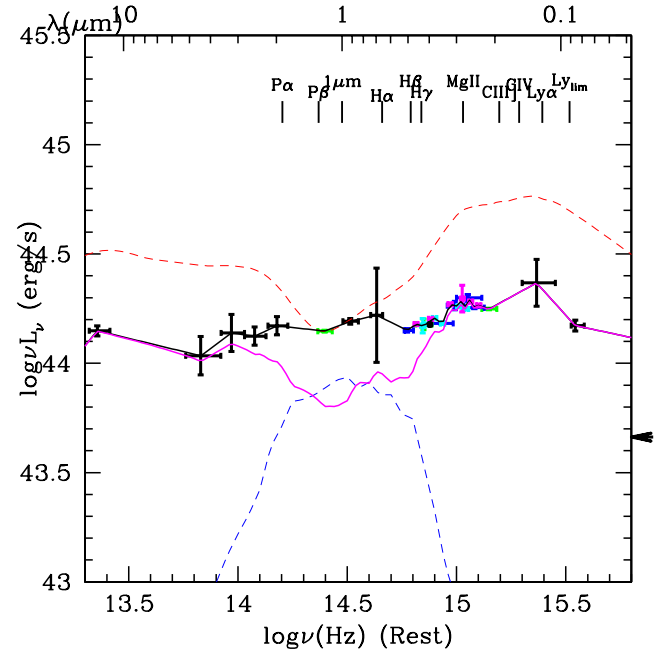


FIG. 18.— SED of source COSMOS_J150.50924+2.699418 (XID=86) at $z=0.794$ (i-band absolute magnitude -22.4). The mass of the black hole is $\log M_{BH} = 8.24$. The black solid line show the SED as the interpolation of the observed data. The magenta solid line shows the SED after host galaxy correction. Red dashed line= E94 RQ mean SED. Blue dashed line=host galaxy template (5Gyr elliptical galaxy) normalized at $L_{J, Gal}$ calculated from the Marconi & Hunt (2003) scaling relationship adding the evolutionary term. The points are color coded as in Figure 8.

Note that, in these formulae, L_{bol} has the same coefficient as λ_E , thus the host galaxy luminosity is physically a function of the black hole mass only (see Marconi & Hunt 2003 for details). To apply these formulae, black

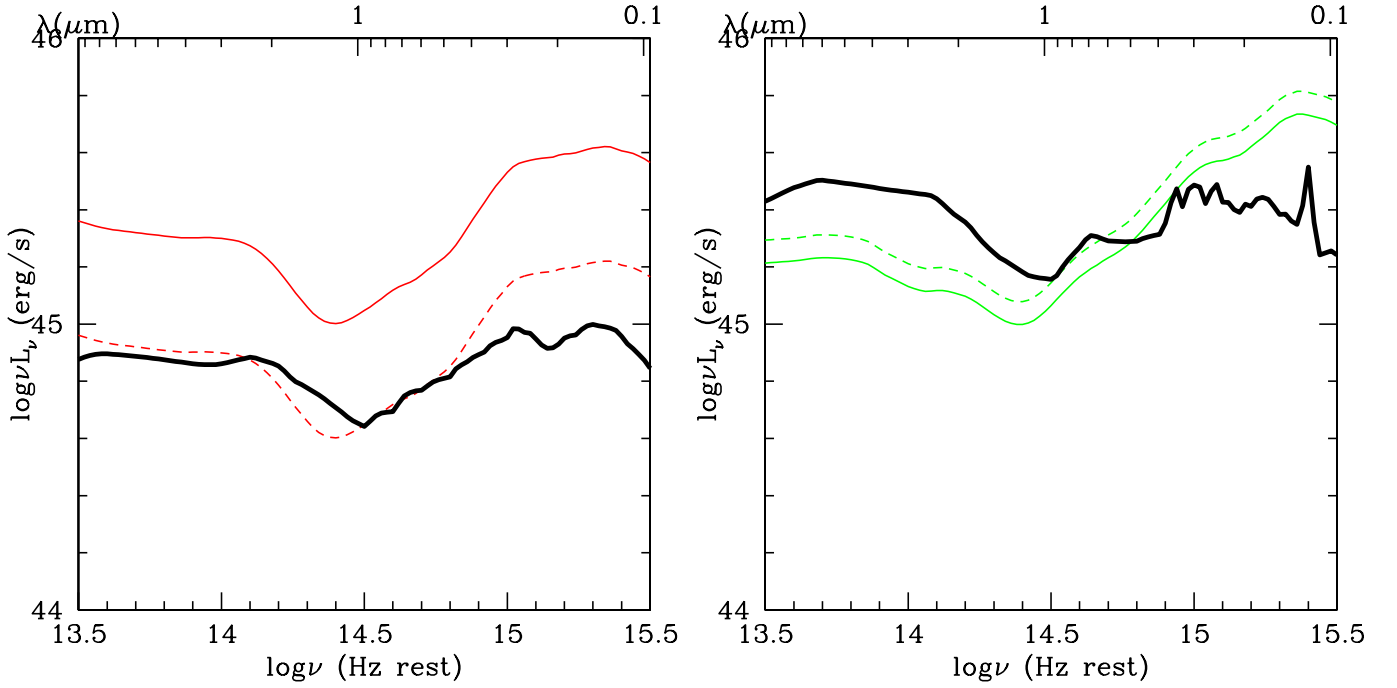


FIG. 19.— *Left*: The mean IR to UV SED for 199 radio quiet (RQ) sources in our sample after all corrections including host galaxy subtraction (black solid line). The red lines are the E94 radio-quiet mean SED (the dashed line is normalized to the XMM sample). *Right*: The mean IR to UV SED for 4 radio loud (RL) quasars after all corrections (black solid line). The green lines are the E94 radio-loud mean SED (dashed is normalized to the XMM sample).

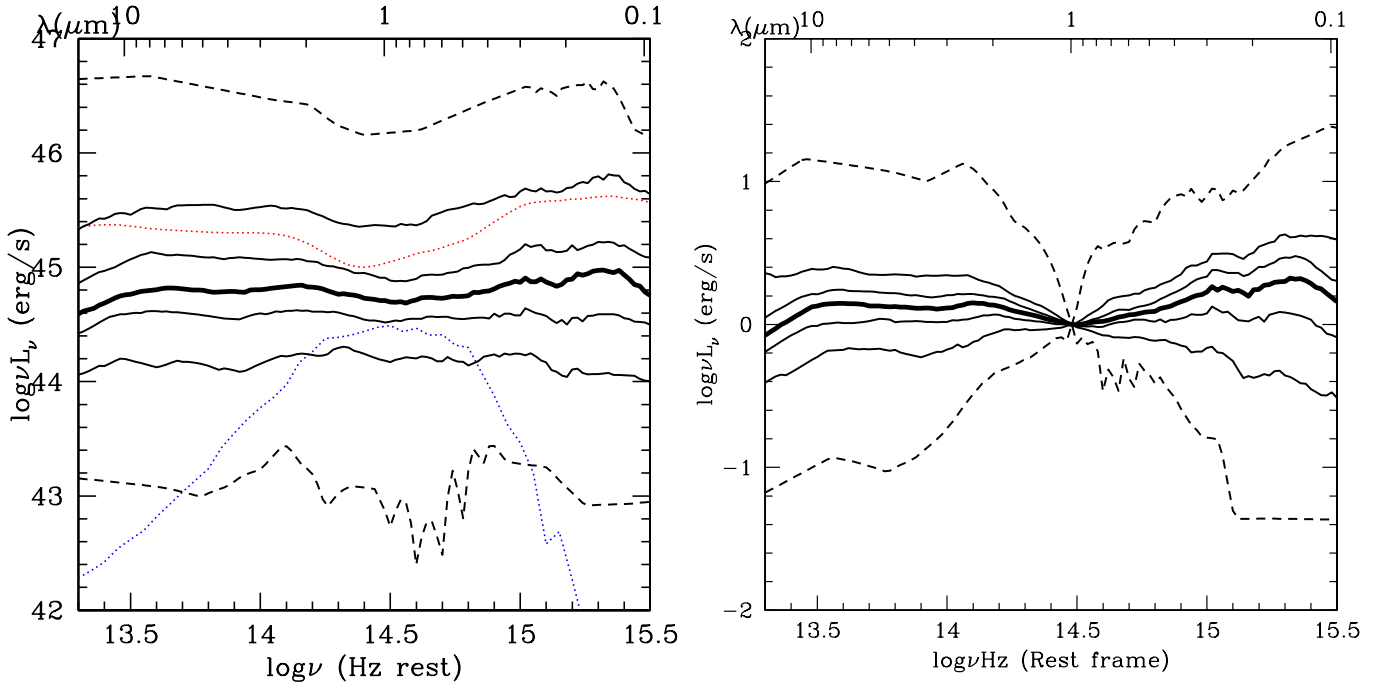


FIG. 20.— The median (thick black line) SED and the 68%, 90% (thin solid black lines) and 100% (dashed black lines) percentile envelopes in the ultraviolet to infrared ($0.9\mu\text{m}$ - $24\mu\text{m}$) range after all correction including the host galaxy subtraction: *Left*: before normalization; *Right*: normalized at $1\mu\text{m}$. Red line= E94 SED. Blue dotted line=5 Gyr elliptical galaxy template (E115).

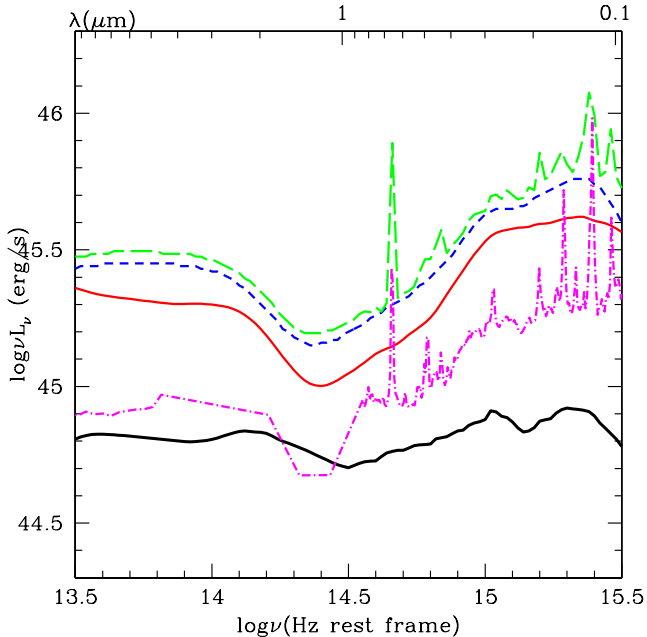


FIG. 21.— The comparison of the mean host-corrected SED for the 199 radio-quiet quasar of XC203 (black solid line) with previous studies. The red solid line shows the E94 radio quiet mean SED. The blue short dashed line shows the Richards et al. (2006) mean SED. The green long dashed line shows the Hopkins et al. (2007) AGN SED template. The magenta dot-dashed line shows the Shang et al. (2011) mean SED.

hole mass estimates are needed. The XC413 quasars have 206 published black hole mass measurements (Trump et al. 2009b; Merloni et al. 2010), which are based on the scaling relationship between BEL FWHM and black hole mass (Vestergaard 2004). For the quasars with only zCOSMOS spectra, the black hole mass was estimated for only the ones with MgII lines in the spectra (Merloni et al. 2010), using the calibration of McLure & Jarvis (2002). For the rest of the sample, the BELs are located at the edge of the spectrum, so that reliable black hole mass estimates cannot be made. We calculated bolometric luminosities by directly integrating the SED from $24\mu\text{m}$ to 40 keV (see Paper 2, Hao et al. 2012 in prep.). The rest-frame J band galaxy luminosity is then calculated using equation (9) for the 206 objects with black hole masses, hereinafter the “XC206” sample.

We need to assume a host galaxy SED to do the corrections. We have no information on the galaxy type of the host for most of the quasars, even with the help of the HST ACS images, as the bulk of the XMM-COSMOS quasars are at $z > 1$. We checked the 16 galaxy templates from the SWIRE template library (Polletta et al. 2007). We normalized all the template to the rest frame J band in Figure 17. We find that none of our quasars show obvious PAH feature in the mid-infrared, which is a prominent feature of starburst galaxy spectra. This could, however, be due to the gap in photometry coverage between the Spitzer bands. From the Spitzer photometry alone, it is difficult to detect such features. Starburst galaxy templates with prominent PAH feature are not suitable for host correction, though, as the PAH feature could exceed the observed (interpolated) SED. The elliptical and spiral galaxies have similar SED shapes from

$0.4\text{--}4\mu\text{m}$, with a dispersion less than 0.1 dex. This wavelength range is where the majority of the host galaxy contribution lies. We checked all spiral or elliptical galaxy templates and the correcting results are similar to each other. Therefore, for the purpose of host correction, it makes no difference which templates to choose.

We used a 5 Gyr old elliptical galaxy template (Polletta et al. 2007) normalized to the rest-frame J band galaxy luminosity, and subtracted the galaxy contribution from the observed SED. An example is shown in Figure 18. In this case, the observed SED is rather flat. After subtracting a scaled host contribution (blue dashed line), the corrected SED (magenta solid line) shows a shape close to that of E94 (red dashed line).

This subtraction is successful in 203 cases in XC206. In just 3 cases (1.46%) we have an over-subtraction problem, and 2 out of the 3 are over-subtracted by less than 0.1 dex. By over-subtraction, we mean the normalized host galaxy SED exceeds the observed SED at certain wavelength range (usually at $\sim 1\mu\text{m}$, where the galaxy contributes the most). If we use the local scaling relationship directly, i.e. without the redshift correction, there would be 34 quasars in which the estimated host flux exceeds the observed flux, leading to larger over-subtraction problem. This suggests that the evolutionary term is needed, and gives some support to the idea that the M- σ relation evolves. The over-subtraction could be due either to dispersion or evolution of the scaling relationship. On the other hand, under-subtraction also happens in the correction, which is more difficult to classify. By under-subtraction, we mean that the correction leaves a flat SED at around $1\mu\text{m}$.

The host correction based on the scaling relationship we applied here is probably not the most accurate, but is the best available at present. We applied this host galaxy correction for these 203 quasars, hereinafter “XC203”. The XC203 quasars are plotted as green hexagons in Figure 2–5. In this sub-sample, four⁴³ are radio-loud according to the criteria discussed in §3.3. We calculated the mean SED and dispersion SED as the previous section.

The mean and dispersion of the XC203 SEDs after all the corrections, including galaxy correction, resembles the E94 mean SED (Figure 19 and 20).

In Figure 21, we compared the mean XC203 SED with other mean SEDs: E94 radio quiet, R06, Hopkins et al. (2007) and the Shang et al. (2011). The R06 SEDs used a “gap-repair” technique, that replace the missing values with normalized the E94 mean SED to the adjacent photometry bands. As the R06 has limited coverage in near infrared J H K bands (J:40/259, H:35/259, K:42/259), the mean SED is therefore, by construction, similar to the E94 radio quiet mean SED. The Hopkins et al. (2007) just combined the R06 mean SED template with the composite quasar SED (Vanden Berk et al. 2001), and so their SED template has a similar shape as R06. The Shang et al. (2011) mean SED is calculated using nearby bright quasars, which have the same selection bias as E94 and so finds a similar shape as E94. Compared to all these SED templates, the XC203 mean SED is flatter due to possible excess host contribution, not corrected because of the dispersion in the scaling relationship itself.

⁴³ XID=5230, 5275, 5517, 54541.

4.5. The Variety of Type 1 AGN SEDs in COSMOS

Simply using the dispersion in the SEDs (Figure 16), does not give a full picture of the variety of SEDs in the XC413 sample. To illustrate the variety of type 1 AGN SEDs found in the XMM-COSMOS sample, we have selected four examples that span the range of properties (Figure 22, A, B, C, D). The four sources are also marked in Figure 2–5. These four examples illustrate:

1. *A. ‘Normal’ SED*, with photometry points lying strikingly close to the E94 radio quiet mean SED (red dashed line), except for the few that are clearly affected by the broad emission lines $H\alpha$, CIV and $Ly\alpha$, and the point beyond the Lyman limit.
2. *B. ‘Reddened’ SED*, with an optical/UV SED too blue to be a host galaxy, but dropping rapidly toward the UV, an effect quite likely caused by reddening. The ~ 1 dex drop in the u-band compared to the E94 RQ mean would correspond to a fairly modest extinction of $E(B-V)=0.18$, for an SMC extinction curve (Gordon et al. 2003).
3. *C. ‘Host dominated’ SED*, matching closely to galaxy templates. The observed SED could be fitted as a strong galaxy plus a faint AGN component. About 10% of the quasars in the sample have host contribution of more than 85% at $\sim 1\mu\text{m}$.
4. *D. ‘Hot-dust-poor’ SED*, lacking a $1\mu\text{m}$ inflection point, but with a normal E94-like strong big blue bump. About 10% of the quasars in the sample belong to this category. These quasars have been discussed in detail in Hao et al. (2010a).

As the variety of the SED shapes in the sample is a continuous distribution, the fraction of the sources of the above four types depend on how we define the selection criteria for each type. Besides, for most of the sources, the SED shape can be explained by combining two or more of the above four types. So the fraction of the sources in each type can not be easily estimated.

Three of these four types have been seen before in AGN at lower redshift, but similar luminosity. The early 2–10 keV sky surveys (e.g. Ariel V, Cooke et al. 1978, HEAO-1 A2, Piccinotti et al. 1982) produced samples of a few dozen AGN that have similar SED characteristics. Ward et al. (1987) compiled U-band to IRAS $100\mu\text{m}$ SEDs for the ‘Piccinotti’ AGN and divided them into three types based on their $f(60\mu\text{m})/f(12\mu\text{m})$ to $f(1.2\mu\text{m})/f(0.36\mu\text{m})$ flux ratios: (A) prominent big blue bump objects (e.g. 3C 273), which correspond to the ‘Normal’, E94-like, objects; (B) rapidly dropping optical SEDs with no strong FIR emission (e.g. MCG-6-30-15), which are reddened AGN and resemble the ‘No Big Bump’ objects; (C) strong FIR, weak optical/UV objects (e.g. NGC 3227), which are dominated by host galaxy emission in both regions and so correspond to the ‘Host dominated’ objects. The host FIR emission in Class C AGN is often extended and lies in the range of normal galaxies in 50% of cases, and of starbursts in the rest.

In a companion paper (Carleton et al. 1987) the same authors argued that all of these types were consistent with a single intrinsic form of the quasar SED, modified only by obscuration and host galaxy contamination.

The bluest of the Class A objects would exhibit this SED form, which is close to the E94 mean SED. Many of the ‘reddened Class B’ objects have X-ray column densities $N_H \sim 10^{22}\text{--}10^{23}\text{ cm}^{-2}$, and have intermediate AGN types (1.5, 1.8, 1.9 Osterbrock & Koski 1976) indicating modest reddening of the broad emission line region and continuum of $A_V \sim 0.5\text{--}3$. We do not have $H\alpha/H\beta$ ratios, or X-ray N_H values, for more than a handful of the COSMOS type 1 AGN sample and so cannot yet test whether the XMM-COSMOS sample shares these properties with the Piccinotti AGN. We explore the AGN-host-reddening parameter space in detail in Paper 3.

The fourth class, D. “hot-dust-poor”, has not been recognized before. The missing inflection point is apparently due to the reduced ‘hot dust’ bump by at least a factor 3 in the near-IR. As the hot dust emission is attributed to the ‘torus’ invoked in unified models of AGN to explain the type 1/type 2 dichotomy, the existence of a class of AGN without this ‘torus’ emission raises questions about the universality of the unified model. This class of sources are discussed in detail in Hao et al. (2010) for COSMOS and Hao et al. (2011a) for optically selected samples.

5. SUMMARY & CONCLUSIONS

In this paper we have assembled a large sample of 413 type 1 AGN (emission line FWHM $> 2000\text{ km s}^{-1}$), selected in X-rays by *XMM-Newton* within the COSMOS field. The sample includes sources with spectroscopic redshifts and a uniform multiwavelength coverage from the X-ray to the far infrared, with 33.6% radio (VLA) coverage too.

We briefly analyzed the optical and X-ray properties of the sample with the main aim to compare them with the Elvis et al. (1994) sample, which is our reference for the construction of the mean SED.

The main goal of this paper is to derive the mean Type 1 AGN SED. We have derived SEDs for all the 413 type 1 AGN. For 203 sources, we could use the black hole mass and the $M_{BH} - M_{bulge}$ scaling relation to produce host-subtracted SEDs. The COSMOS type 1 AGN sample spans a much larger range of redshift and luminosity than the E94 sample. Only 6 of these AGN, $\sim 1.5\%$, are radio-loud.

These SEDs make use of the vast COSMOS photometric data set, and so contain many photometric points (a mean of 35 per SED). The SEDs are especially well sampled in the optical/UV band ($\sim 0.1 - 1\mu\text{m}$), with a mean of 18 photometric points. We have corrected the SEDs for Galactic extinction, have restricted the data collection time interval to limit variability and have made a correction for the BEL contribution. The SEDs were re-sampled on a uniform rest frame frequency grid.

The mean SED in the rest frame $8\mu\text{m}$ to 4000\AA are calculated based on detections only. Mean SED beyond this range are calculated based on reasonable power law assumption. The mean SED of the sample before host galaxy correction is quite different from the E94 mean radio-quiet SED and does not show a prominent $1\mu\text{m}$ inflection point between the UV and near-IR bumps. Sub-samples of AGN (with black hole mass estimation) corrected for host galaxy contribution using the Marconi & Hunt (2003) scaling relationship, with an additional redshift evolution term, restores the $1\mu\text{m}$ inflection to

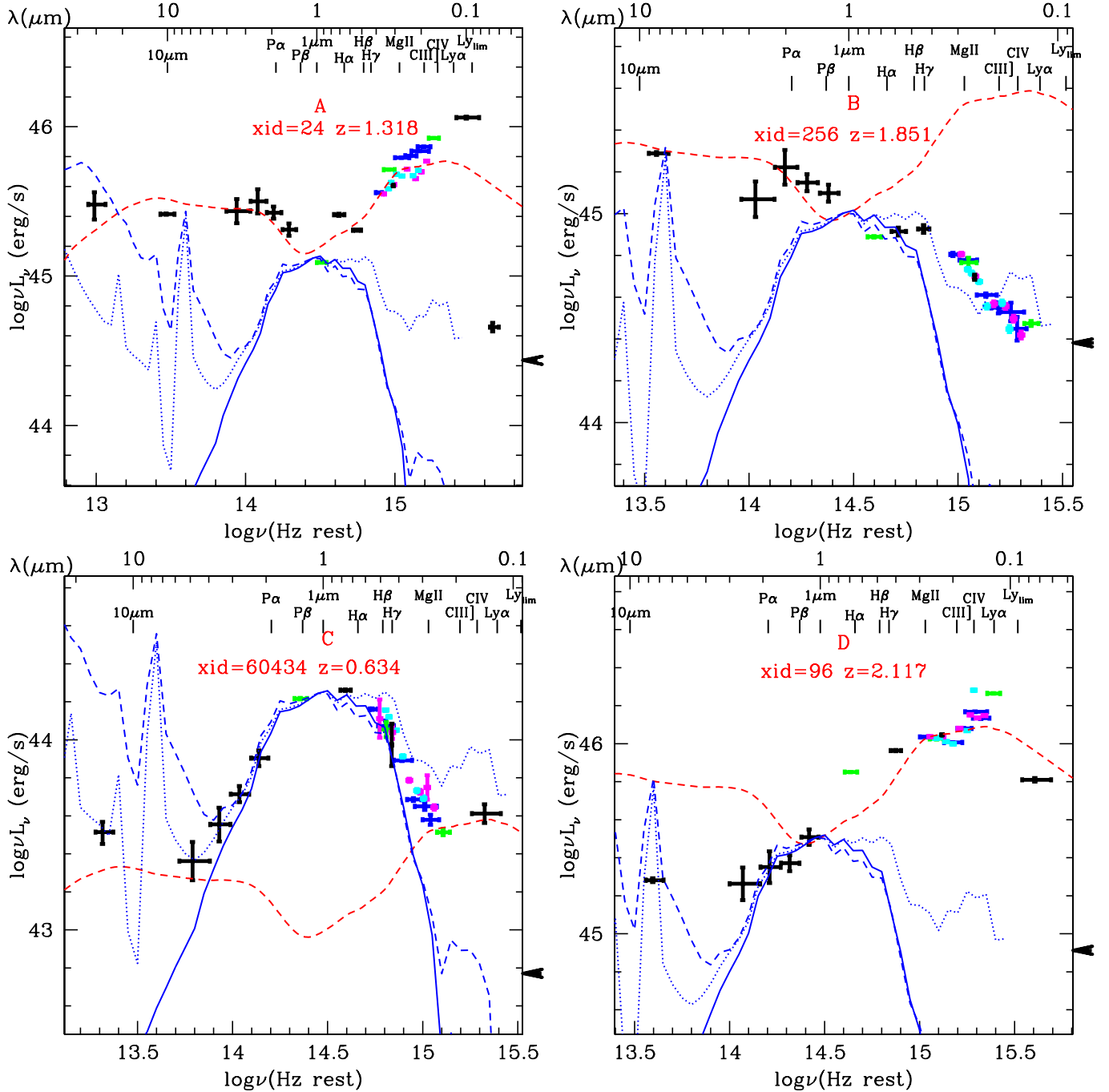


FIG. 22.— Extreme examples of SEDs: *top left*: A. a close analog of the E94 mean SED; *top right*: B. no big blue bump, probably due to reddening and/or a strong galaxy component; *bottom left*: C. a probable galaxy dominated AGN. ; *bottom right*: D. strong big blue bump but no $1 \mu\text{m}$ inflection due to a weak near-IR bump. The data points and the E94 RQ SED are shown as in Figure 8. The galaxy templates are shown as in Figure 14 normalized at $1 \mu\text{m}$.

the mean COSMOS type 1 SED. This shows that host galaxy contamination is likely to be a major contributor to the variety of SEDs in an X-ray selected sample. Evolution of the $M\text{-}\sigma$ relation is supported by the better host subtraction obtained using the Bennert et al. (2011) relation.

The SEDs before and after the corrections for the Galactic extinction, for broad emission line contributions, constrained variability, and for host galaxy contribution are available on-line at the journal web site.

Both host contamination and reddening for all COSMOS quasars will be addressed in companion papers (Hao et al. 2012 in prep.).

Several extreme types of AGN SED were identified, corresponding to an E94 SED, a reddened E94 SED and a host dominated SED. These three SED types have been seen previously (e.g. Ward et al. 1985). A new sub-class of ‘hot-dust-poor’ quasars has been found that appears to lack strong hot dust emission. These will be of interest for unification models as they appear to indicate the ab-

sence of the standard obscuring ‘torus’. Their properties are discussed in Hao et al. (2010, 2011a).

The COSMOS AGN photometry coverage continues to expand. In particular the far-infrared to millimeter region: Far-IR (60-600 μ m) has been observed with the *Herschel* satellite, SCUBA2 will image the field at 850 μ m and 1.1 mm imaging of much of the field by AzTeC has been performed and should yield several hundred sources (Scott et al. 2008, Austermann et al. 2009). The quasar SED properties over wider wavelength ranges will be possible in the near future.

ACKNOWLEDGMENTS

ME and HH thank J. McDowell for useful discussion. This work was supported in part by NASA *Chandra* grant number GO7-8136A (HH, FC, ME),

NASA contract NAS8-39073 (Chandra X-ray Center) and the Smithsonian Scholarly Studies (FC). KJ acknowledges support from the Emmy Noether Programme of the German Science Foundation (DFG) through grant number JA 1114/3-1. In Italy this work is supported by ASI/INAF contracts I/009/10/0, I/024/05/0 and I/088/06. In Germany this project is supported by the Bundesministerium für Bildung und Forschung/Deutsches Zentrum für Luft und Raumfahrt and the Max Planck Society. MS and GH acknowledge support bei the Leibniz Prize of the Deutsche Forschungsgemeinschaft, DFG (HA 1850/28-1). YL acknowledges partial funding support by the Directional Research Project of the Chinese Academy of Sciences under project no. KJCX2-YW-T03 and by the National Natural Science Foundation of China under grant nos. 10821061, 10733010, 10725313, and by 973 Program of China under grant 2009CB824800.

REFERENCES

- Abazajian, K. N., et al., 2004, *AJ*, 128, 502
 Abazajian, K. N., et al., 2009, *ApJS*, 182, 543
 Allen, C. W. 1976, *Astrophysical Quantities* (University of London, The Athlone Press)
 Appleton, P. N., et al., 2004, *ApJS*, 154, 147
 Arnaud, K. A., 1996, *ASPC*, 101, 17
 Austermann, J. E., et al., 2009, *MNRAS*, 393, 1573
 Avni, Y. & Tananbaum, H., 1986, *ApJ*, 305, 83
 Baldwin, J. A., 1977, *ApJ*, 214, 679
 Bolzonella, M., Miralles, J. M., & Pelló, R., 2000, *A&A*, 363, 476
 Brissenden, R. J. V., 1989, PhD thesis
 Brusa, M., et al., 2005, *A&A*, 2005, 421, 69
 Brusa, M., et al., 2007, *ApJS*, 2007, 172, 353
 Brusa, M., et al., 2010, *ApJ*, submitted
 Capak, P., et al., 2007, *ApJS*, 172, 99
 Capak, P., et al., 2010, in preparation
 Cappelluti, N., et al., 2007, *ApJS*, 172, 341
 Cappelluti, N., et al., 2009, *A&A* submitted, arXiv:0901.2347
 Cardelli, J. A., Clayton, G. C. & Mathis, J. S., 1989, *ApJ*, 345, 245
 Carleton, N. P., et al., 1987, *ApJ*, 318, 595
 Cirasuolo, M., et al., 2007, *MNRAS*, 380, 585
 Cirasuolo, M., et al., 2003, *MNRAS*, 341, 993
 Cisternas, M., et al., 2011, *ApJ*, 726, 57
 Civano, F., Elvis, M., Brusa, M., et al., 2012, arXiv:1205.5030
 Cooke, B. A., et al., 1978, *MNRAS*, 182, 489
 Dickey, J. M. & Lockman, F. J., 1990, *ARA&A*, 28, 215
 Donley, J. L. et al. 2012, *ApJ*, 748, 142
 Dunne, L. & Eales, S. A., 2001, *MNRAS*, 327, 697
 Eisenstein, D. J., et al., 2001, *AJ*, 122, 2267
 Elvis, M. et al., 1994, *ApJS*, 95, 1
 Elvis, M., Risaliti, G., & Zamorani, G., 2002, *ApJ*, 565, L75
 Elvis, M. et al., 2009, *ApJS*, 184, 158
 Eskridge, P. B., Fabbiano, G., & Kim, Dong-Woo, 1995, *ApJ*, 448, 70
 Falter, S. et al., 2004, *Outskirts of Galaxy Clusters: Intense Life in the Suburbs*, 233
 Ferland, G. J. and Osterbrock, D. E., 2005, *Astrophysics of Gaseous Nebulae and Active Galactic Nuclei*, Univ Science Books
 Frayer, D. T. et al., 2009, *AJ*, 138, 1261
 Gabor, J. M. et al., 2009, *ApJ*, 691, 705
 Gilli, R., Comastri, A. & Hasinger, G., 2007, *A&A*, 463, 79
 Gordon, K. et al., 2003, *ApJ*, 594, 279
 Green, P. et al., 2001, *ApJ*, 556, 727
 Hao, H., et al., 2010a, *ApJ*, 724, L59
 Hao, H., et al., 2011, *ApJ* 733, 108
 Hao, H., et al., 2012a, *MNRAS* submitted.
 Hao, H., et al., 2012b, *MNRAS* submitted.
 Hao, H., et al., 2012c, *ApJ* Letter submitted.
 Hasinger, G., et al., 2007, *ApJS*, 172, 29
 Hasinger, G., 2008, *A&A*, 490, 905
 Hawkins, S. E., et al., 2007, *A&A*, 462, 581
 Hooper, E. J., et al., 1996, *ApJ*, 473, 746
 Hopkins, P. F., et al., 2006, *ApJS*, 163, 1
 Hopkins, P. F., et al., 2004, *ApJ*, 128, 1112
 Ilbert, O., et al., 2009, *ApJ*, 690, 1236
 Ivezić, Ž., 2004, in *Multiwavelength AGN Surveys*, ed. R. Mújica & R. Maiolino (Singapore: World Scientific), 53
 Ivezić, Ž., et al., 2002, *AJ*, 124, 2364
 Just, D. W., Brandt, W. N. et al., 2007, *ApJ*, 665, 1004
 Kartaltepe, J., et al., 2010, *ApJ*, 709, 572
 Kellermann, K. I., et al., 1989, *AJ*, 98, 1195
 Kelly, B. C., Bechtold, J., Trump, J. R., Vestergaard, M., Siemiginowska, A., 2008, *ApJS*, 176, 355
 Koekemoer, A. M., et al., 2007, *ApJs*, 172, 196
 Komatsu, E., et al., 2009, *ApJS*, 180, 330
 Kuraszkievicz, J. K., et al., 2003, *ApJ*, 590, 128
 La Franca, F., et al. 2005, *ApJ*, 635, 864
 Lapi, A. et al. 2011, *ApJ*, 742, 24
 Lawrence, A., & Elvis, M., 1982, *ApJ*, 256, L410
 Le Floch, E. et al., 2009, *ApJ*, 703, 222L
 Lilly, S. J., et al., 2007, *ApJS*, 172, 70
 Lilly, S. J., et al., 2009, *ApJS*, 184, 218
 Luo, B., et al., 2010, *ApJS*, 187, 560
 Lusso, E., et al., 2010, *A&A* 512, 34
 Magorrian, J., et al., 1998, *AJ*, 115, 2285
 Mainieri, V., et al., 2007, *ApJS*, 172, 368
 Maiolino, R., et al., 2007, *A&A*, 468, 979
 Marconi, A. & Hunt, L. K. 2003, *ApJ* 589, L21
 Marconi, A., et al., 2004, *MNRAS*, 351, 169
 McCracken, H. J., et al., 2007, *ApJS*, 172, 314
 McCracken, H. J., et al., 2010, *ApJS*, 708, 202
 McLeod, K. K. & Rieke, G. H., 1994, *ApJ*, 431, 137
 McLure, R. J. & Jarvis, M. J., 2002, *MNRAS*, 337, 109
 Merloni, A., et al., 2010, *ApJ* 708, 137
 Miller, L., et al., 1990, *MNRAS*, 244, 207
 Osterbrock, D. E. & Koski, A. T., 1976, *MNRAS*, 176P, 61
 Oke, J. B. & Gunn, J. E., 1983, *ApJ*, 266, 713
 Peterson, B. M. et al., 2004, *ApJ*, 613, 682
 Peterson, B. M., 1997, *An Introduction to Active Galactic Nuclei* (Cambridge: Cambridge University Press)
 Piccinotti, G., et al., 1982, *ApJ*, 253, 485
 Polletta, M., et al., 2000, *A&A*, 362, 75
 Polletta, M., et al., 2007, *ApJ*, 663, 81
 Puchnarewicz, E. M., et al., 1997, *MNRAS* 291, 177
 Richards, G. T., et al., 2006, *ApJ*, 166, 470
 Risaliti, G. & Elvis, M., 2004, in *ASSL Vol 308, Supermassive Black Holes in the Distant Universe*, ed. A. J. Barger (Dordrecht: Kluwer), 187
 Rosati, P. et al., 2002, 566, 667
 Salvato, M., et al., 2009, *ApJ*, 690, 1250
 Sanders, D. B., et al., 2007, *ApJS*, 172, 86
 Sargent, M. T., et al. 2010, *ApJS*, 186, 341
 Schinnerer, E., et al., 2007, *ApJS*, 172, 46
 Schinnerer, E., et al., 2010, *ApJS*, 188, 384.
 Schlegel, D. J., et al., 1998, *ApJ*, 500, 525
 Schmidt, M. & Green, R. F., 1983, *ApJ*, 269, 352
 Schneider, D. P., et al., 2007, *AJ*, 130, 367
 Scodreggio, M., et al., 2005, *PASP*, 117, 1284
 Scott, K. S., et al., 2008, *MNRAS*, 385, 2225
 Scoville, N. Z., et al., 2007, *ApJS*, 172, 1
 Scoville, N. Z., et al., 2007, *ApJS*, 172, 38
 Sergeev, S. G., et al., 2006, *ASPC*, 360, 13
 Shang, Z., et al., 2007, *ApJ*, 134, 294
 Shang, Z., et al., 2011, *ApJS*, 196, 2
 Sikora, M., Stawarz, L. & Lasota, J. P., 2007, *ApJ*, 658, 815
 Spergel, D. N., et al., 2007, *ApJS*, 170,377

- Steffen, A. T., et al., 2003, *ApJL*, 563, 23
Steffen, A. T., Strateva, I., et al., 2006, *AJ*, 131, 2826
Strateva, I. V., Brandt, W. N., et al., *AJ*, 130, 387
Sutherland, W. & Sanders, W., 1992, *MNRAS*, 259, 413
Tananbaum, H., et al., 1979, *ApJ*, 234, 9
Taniguchi, Y., et al., 2007, *ApJS*, 172, 9
Treister, E., & Urry, C. M. 2005, *ApJ*, 630, 115
Treister, E., & Urry, C. M. 2006, *ApJ*, 652, L79
Tremaine, S., et al. 2002, *ApJ*, 574, 740
Trump, J. R., et al., 2007, *ApJS*, 172, 383
Trump, J. R., et al., 2009, *ApJ*, 696, 1195
Trump, J. R., et al., 2009, *ApJ*, 700, 49
Trump, J. R., et al., 2011, *ApJ*, 733, 60
Ueda, Y., et al., 2003, *ApJ*, 598, 886
Urry, C. M. & Padovani, P., 1995, *PASP*, 107, 803
Vanden Berk, D. E., et al., 2001, *AJ*, 122, 549
Vanden Berk, D. E., et al., 2004, *ApJ*, 601, 692
Vanden Berk, D. E., et al., 2006, *AJ*, 131, 84
Vestergaard, M. & Peterson, B. M., 2003, *ApJ*, 641, 689
Vestergaard, M., 2004, *ApJ*, 601, 676
Vestergaard, M., 2002, *ApJ*, 571, 733
Visnovsky, K. L., et al., 1992, *ApJ*, 391, 560
Wilkes, B. J. & Elvis, M., 1987, *ApJ*, 323, 243
Wilkes, B. J., 2003, *ASPC*, 311, 37
Ward, M. J., 1987, *ApJ* 315,74
Xue, Y. Q., et al., 2010, *ApJ*, 720, 368
York, D., 2000, *AJ*, 120, 1579
Young, M., Elvis, M., Risaliti, G., 2010, *AJ*, 708, 1388
Zakamska, N. L., et al., 2003, *AJ*, 126, 2125
Zamojski, M. A., et al., 2007, *ApJS*, 172, 468
Zamorani, G., Henry, J.P., Maccararo, T., et al. 1981, *ApJ*, 245, 357
Zatloukal, M., et al., 2007, *A&A*, 474, 5